Supplementary information for the paper:

Distinct roles of fast, slow, and unobservable relaxation regimes controlling proton transport barriers in lanthanide metal–organic coordination polymers featuring hexameric water clusters

Xingru Wu, [a] *Fengxia Xie,* [*a] *Chengan Wan,* [b] *Bingtang Chen, Yifeng Jia,* [a] *Hejia Ji,* [a] *Pingping Li,* [a] *Feng Zhang,* [c] *Lei Feng,* [b] *Chen Wen* [*b] *and Xiaoqiang Liang,* [*a]

[a] *College of Environmental and Chemical Engineering, Xi'an Polytechnic University, Xi'an 710048, PR China. E-mail: anxiny@163.com, xq-liang@163.com*

[b] *Beijing Spacecrafts, Beijing 100094, PR China. E-mail: 13552907280@163.com*

[c] *Key Laboratory of Photochemical Biomaterials and Energy Storage Materials, Heilongjiang Province and College of Chemistry and Chemical Engineering, Harbin Normal University, Harbin 150025, PR China.*

Table of Contents

I. Crystallographic data

Table S1 Crystallographic data and details of refinements for **Pr-Ce-H_2pda-H_2O**, **Pr-Hpda-H_2O** and **Pr-pda-H_2O** [1–3]

Compounds	Pr-Ce-H_2pda-H_2O	Pr-Hpda-H_2O	Pr-Ppad-H_2O
Empirical formula	$C_{28}H_{35}CeN_4O_{28}Pr$	$C_{14}H_{27}N_2O_{18}Pr$	$C_{21}H_{19}N_3O_{16}Pr_2$
M_r	1140.62	580.22	849.2
Crystal system	triclinic	monoclinic	monoclinic
Space group	*P−1*	$P2_1/c$	$P2_1/c$
a (Å)	12.787(2)	14.127(5)	10.9850(7)
b (Å)	13.112(2)	11.308(4)	17.5385(12)
c (Å)	13.121(2)	13.020(5)	13.4684(9)
α (°)	97.608(2)	90	90
β (°)	91.111(2)	101.972(5)	101.041(2)
γ (°)	118.973(2)	90	90
V (Å^3)	1898.8(5)	2034.7(13)	2546.8(3)
Z	2	4	4
D_c (g cm^{-3})	2.023	1.894	2.220
μ (mm^{-1})	2.563	2.471	3.869
F (000)	1144	1152	1648.0

Table S2 Selected bond lengths (Å) and angles (°) for **Pr-Ce-H_2pda -H_2O**, **Pr-Hpda-H_2O** and **Pr-pda-H_2O** [1–3]

	Pr-Ce-H_2pda-H_2O		
Pr−O(32)	2.454(3)	Pr−O(41)	2.445(3)
Pr−O(43)	2.476(3)	Pr−O(51)	2.583(3)
Pr−O(52)	2.511(4)	Pr−O(53)	2.505(3)
Pr−O(54A)	2.703(11)	Pr−O(54B)	2.604(12)
Pr−N(41)	2.584(3)	Pr−O(22a)	2.479(2)
Ce−O(11)	2.347(3)	Ce−O(13)	2.312(3)
Ce−O(21)	2.408(3)	Ce−O(23)	2.383(3)
Ce−O(31)	2.340(3)	Ce−O(33)	2.384(3)
Ce−N(11)	2.485(3)	Ce−N(21)	2.539(3)
Ce−N(31)	2.517(2)	O(32)−Pr−O(41)	93.81(11)
O(51)−Pr−N(41)	69.25(11)	O(32)−Pr−O(43)	73.67(10)
O(22a)−Pr−O(51)	70.29(9)	O(32)−Pr−O(51)	140.43(10)
O(52)−Pr−O(53)	89.93(11)	O(32)−Pr−O(52)	139.21(11)
O(52)−Pr−O(54A)	77.6(2)	O(32)−Pr−O(53)	74.59(11)
O(52)−Pr−O(54B)	64.0(2)	O(32)−Pr−O(54A)	62.1(2)
O(52)−Pr−N(41)	127.65(11)	O(32)−Pr−O(54B)	75.4(2)
O(22a)−Pr−O(52)	73.32(12)	O(32)−Pr−N(41)	71.85(10)
O(53)−Pr−O(54A)	74.9(3)	O(22)−Pr−O(32)	129.86(11)
O(53)−Pr−O(54B)	63.4(3)	O(41)–Pr–O(43)	124.78(9)
O(53)–Pr–N(41)	141.85(13)	O(41)–Pr–O(51)	74.46(11)
O(22a)–Pr–O(53)	67.70(10)	O(41)–Pr–O(52)	72.84(10)
O(54A)–Pr–O(54B)	19.2(4)	O(41)–Pr–O(53)	138.23(11)
O(54A)–Pr–N(41)	104.1(3)	O(41)–Pr–O(54A)	64.5(3)
O(22a)–Pr–O(54A)	131.9(3)	O(41)–Pr–O(54B)	74.9(3)
O(54B)–Pr–N(41)	122.9(3)	O(41)–Pr–N(41)	62.32(11)
O(22a)–Pr–O(54B)	113.0(3)	O(22a)–Pr–O(41)	136.31(12)
O(22a)–Pr–N(41)	124.02(10)	O(43)–Pr–O(51)	82.37(11)
O(11)–Ce–O(13)	128.48(9)	O(43)–Pr–O(52)	145.43(10)
O(11)–Ce–O(21)	82.90(11)	O(43)–Pr–O(53)	90.91(11)
O(11)–Ce–O(23)	80.55(10)	O(43)–Pr–O(54A)	135.6(2)
O(11)–Ce–O(31)	80.13(9)	O(43)–Pr–O(54B)	144.1(2)
O(11)–Ce–O(33)	146.39(9)	O(43)–Pr–N(41)	62.68(11)
O(11)–Ce–N(11)	63.96(11)	O(22a)–Pr–O(43)	75.11(10)
O(11)–Ce–N(21)	77.19(11)	O(51)–Pr–O(52)	74.07(11)
O(11)–Ce–N(31)	138.49(9)	O(51)–Pr–O(53)	137.78(10)
O(13)–Ce–O(21)	81.51(10)	O(51)–Pr–O(54A)	135.3(2)
O(13)–Ce–O(23)	145.02(9)	O(51)–Pr–O(54B)	133.6(2)
O(13)–Ce–O(31)	90.22(9)	O(13)–Ce–O(33)	76.03(9)
O(13)–Ce–N(11)	64.55(11)	O(13)–Ce–N(21)	134.29(12)
O(13)–Ce–N(31)	73.63(9)	O(21)–Ce–O(23)	126.14(9)
O(21)–Ce–O(31)	150.30(9)	O(21)–Ce–O(33)	78.44(10)

O(21)–Ce–N(11)	73.52(11)	O(21)–Ce–N(21)	63.18(10)
O(21)–Ce–N(31)	138.47(11)	O(23)–Ce–O(31)	74.66(9)
O(23)–Ce–O(33)	88.19(11)	O(23)–Ce–N(11)	137.72(13)
O(23)–Ce–N(21)	63.25(10)	O(23)–Ce–N(31)	71.39(9)
O(31)–Ce–O(33)	127.24(8)	O(31)–Ce–N(11)	77.16(11)
O(31)–Ce–N(21)	134.64(11)	O(31)–Ce–N(31)	63.54(9)
O(33)–Ce–N(11)	134.09(12)	O(33)–Ce–N(21)	69.48(11)
O(33)–Ce–N(31)	63.71(8)	N(11)–Ce–N(21)	124.40(11)
N(11)–Ce–N(31)	121.44(10)	N(21)–Ce–N(31)	114.08(9)
O(11)–C(17)	1.281(5)	O(12)−C(17)	1.236(7)
O(13)−C(16)	1.284(5)	O(14)−C(16)	1.227(5)
O(21)−C(27)	1.264(4)	O(22)−C(27)	1.238(5)
O(23)−C(26)	1.264(5)	O(24)−C(26)	1.227(6)
O(31)−C(37)	1.269(4)	O(32)−C(37)	1.229(5)
O(33)−C(36)	1.268(4)	O(34)−C(36)	1.234(6)
O(41)−C(47)	1.243(6)	O(42)−C(47)	1.266(7)
O(43)−C(46)	1.251(5)	O(44)−C(46)	1.267(5)
Pr-Hpda-H_2O			
Pr(1)−O(1)	2.110(2)	Pr(1)−O(3)	2.560(2)
Pr(1)−O(5)	2.570(2)	Pr(1)−O(7)	2.496(2)
Pr(1)−O(9)	2.462(2)	Pr(1)−O(10)	2.493(2)
Pr(1)−N(1)	2.630(2)	Pr(1)−N(2)	2.636(3)
Pr(1)−O(4a)	2.495(2)	O(1)–Pr(1)–O(3)	122.14(7)
O(9)–Pr(1)–N(2)	133.63(7)	O(1)–Pr(1)–O(5)	81.55(7)
O(4a)–Pr(1)–O(9)	72.39(7)	O(1)–Pr(1)–O(7)	153.22(7)
O(10)–Pr(1)–N(1)	123.95(9)	O(1)–Pr(1)–O(9)	86.08(8)
O(10)–Pr(1)–N(2)	73.93(8)	O(1)–Pr(1)–O(10)	78.33(8)
O(4a)–Pr(1)–O(10)	70.32(9)	O(1)–Pr(1)–N(1)	61.63(7)
N(1)–Pr(1)–N(2)	111.82(7)	O(1)–Pr(1)–N(2)	138.95(7)
O(4a)–Pr(1)–N(1)	129.62(7)	O(1)–Pr(1)–O(4a)	78.23(7)
O(4a)–Pr(1)–N(2)	118.48(7)	O(3)–Pr(1)–O(5)	82.80(7)
O(3)–Pr(1)–O(7)	75.66(7)	O(3)–Pr(1)–O(9)	72.53(7)
O(3)–Pr(1)–O(10)	144.63(8)	O(3)–Pr(1)–N(1)	61.13(7)
O(3)–Pr(1)–N(2)	72.55(7)	O(3)–Pr(1)–O(4a)	137.51(7)
O(5)–Pr(1)–O(7)	122.89(7)	O(5)–Pr(1)–O(9)	140.58(7)
O(5)–Pr(1)–O(10)	71.44(9)	O(5)–Pr(1)–N(1)	65.59(7)
O(5)–Pr(1)–N(2)	61.32(7)	O(4a)–Pr(1)–O(5)	139.51(7)
O(7)–Pr(1)–O(9)	80.58(7)	O(7)–Pr(1)–O(10)	98.10(9)
O(7)–Pr(1)–N(1)	135.08(7)	O(7)–Pr(1)–N(2)	61.86(7)
O(4a)–Pr(1)–O(7)	75.63(7)	O(9)–Pr(1)–O(10)	141.74(8)
O(9)–Pr(1)–N(1)	75.57(8)	O(1)−C(7)	1.271(4)
O(2)−C(7)	1.249(4)	O(3)−C(1)	1.268(4)
O(4)−C(1)	1.252(3)	O(5)−C(8)	1.227(4)
O(6)−C(8)	1.299(4)	O(7)−C(14)	1.263(4)

O(8)−C(14)	1.249(4)		
Pr-pda-H_2O			
Pr(1)–O(1)	2.489(2)	Pr(1)–O(2)	2.565(2)
Pr(1)–O(4)	2.479(2)	Pr(1)–O(7)	2.535(2)
Pr(1)–O(8)	2.365(2)	Pr(1)–N(3)	2.601(2)
Pr(1)–O(13a)	2.391(2)	Pr(1)–O(5b)	2.356(2)
Pr(2)–O(3)	2.5859(19)	Pr(2)–O(9)	2.490(2)
Pr(2)–O(11)	2.558(2)	Pr(2)–O(12)	2.542(2)
Pr(2)–O(15)	2.465(2)	Pr(2)–N(1)	2.604(2)
Pr(2)–N(2)	2.643(2)	Pr(2)–O(6c)	2.463(2)
Pr(2)–O(11d)	2.5747(19)	O(1)–Pr(1)–O(2)	68.90(7)
O(3)–Pr(2)–O(9)	139.87(7)	O(1)–Pr(1)–O(4)	71.95(8)
O(3)–Pr(2)–O(11)	80.70(6)	O(1)–Pr(1)–O(7)	147.48(7)
O(3)–Pr(2)–O(12)	136.82(6)	O(1)–Pr(1)–O(8)	132.97(7)
O(3)–Pr(2)–O(15)	74.47(6)	O(1)–Pr(1)–N(3)	124.72(8)
O(3)–Pr(2)–N(1)	116.98(7)	O(1)–Pr(1)–O(13a)	72.94(8)
O(3)–Pr(2)–N(2)	126.54(7)	O(1)–Pr(1)–O(5b)	90.67(9)
O(3)–Pr(2)–O(6c)	70.66(6)	O(2)–Pr(1)–O(4)	92.48(7)
O(3)–Pr(2)–O(11d)	66.91(6)	O(2)–Pr(1)–O(7)	130.81(7)
O(9)–Pr(2)–O(11)	122.36(7)	O(2)–Pr(1)–O(8)	69.18(7)
O(9)–Pr(2)–O(12)	82.96(7)	O(2)–Pr(1)–N(3)	138.39(7)
O(9)–Pr(2)–O(15)	77.60(7)	O(2)–Pr(1)–O(13a)	137.65(7)
O(9)–Pr(2)–N(1)	72.52(7)	O(2)–Pr(1)–O(5b)	77.57(8)
O(9)–Pr(2)–N(2)	61.80(7)	O(4)–Pr(1)–O(7)	124.03(6)
O(6c)–Pr(2)–O(9)	79.21(7)	O(4)–Pr(1)–O(8)	89.61(8)
O(9)–Pr(2)–O(11d)	150.53(7)	O(4)–Pr(1)–N(3)	62.37(7)
O(11)–Pr(2)–O(12)	76.74(6)	O(4)–Pr(1)–O(13a)	92.66(8)
O(11)–Pr(2)–O(15)	155.08(6)	O(4)–Pr(1)–O(5b)	162.28(8)
O(11)–Pr(2)–N(1)	134.06(7)	O(7)–Pr(1)–O(8)	78.50(7)
O(11)–Pr(2)–N(2)	60.61(6)	O(7)–Pr(1)–N(3)	61.66(7)
O(6c)–Pr(2)–O(11)	83.89(6)	O(7)–Pr(1)–O(13a)	77.85(8)
O(11)–Pr(2)–O(11d)	63.77(6)	O(5e)–Pr(1)–O(7)	72.78(7)
O(12)–Pr(2)–O(15)	123.72(6)	O(8)–Pr(1)–N(3)	77.58(7)
O(12)–Pr(2)–N(1)	61.40(7)	O(8)–Pr(1)–O(13a)	152.83(8)
O(12)–Pr(2)–N(2)	70.94(7)	O(5b)–Pr(1)–O(8)	100.24(10)
O(6c)–Pr(2)–O(12)	140.85(6)	O(13a)–Pr(1)–N(3)	79.56(8)
O(11d)–Pr(2)–O(12)	70.14(6)	O(5b)–Pr(1)–N(3)	133.99(7)
O(15)–Pr(2)–N(1)	62.44(7)	O(5b)–Pr(1)–O(13a)	85.30(10)
O(15)–Pr(2)–N(2)	135.44(7)	O(6c)–Pr(2)–O(15)	85.93(7)
O(11d)–Pr(2)–O(15)	107.13(7)	N(1)–Pr(2)–N(2)	116.42(7)
O(6c)–Pr(2)–N(1)	141.03(7)	O(11d)–Pr(2)–N(1)	83.86(7)
O(6c)–Pr(2)–N(2)	69.91(6)	O(11d)–Pr(2)–N(2)	117.19(7)
O(6c)–Pr(2)–O(11d)	129.58(6)	O(4)−C(1)	1.251(3)
O(5)−C(1)	1.242(3)	O(6)−C(7)	1.249(3)

O(7)−C(7)	1.260(3)	O(8)−C(8)	1.261(3)
O(9)−C(8)	1.246(3)	O(10)−C(14)	1.223(4)
O(11)−C(14)	1.283(3)	O(12)−C(15)	1.258(3)
O(13)−C(15)	1.241(3)	O(14)−C(21)	1.241(4)
O(15)−C(21)	1.253(3)		

Symmetry codes: a) *x*, 1+*y*, *z*; for **Pr-Ce-H_2pda-H_2O;** a) *x*, 1/2−*y*, −1/2+*z*; for **Pr-Hpda-H_2O;** a) −1+*x* , *y*, *z*; *b*) *x*, 1/2−*y*, 1/2+*z*; c) 1−*x*, 1−*y*, 1−*z*; d)2−*x*, 1−*y*, 1−*z*; e) 1+*x*, *y*, *z*; for **Pr-pda-H_2O**.

Table S3 Hydrogen−bonding geometry parameters (Å, °) for **Pr-Ce-H_2pda-H_2O**, **Pr-Hpda-H_2O** and **Pr-pda-H_2O** [1–3]

D−H···A	d(D−H)	d(H···A)	d(D···A)	∠(DHA)
Pr-Ce-H_2pda-H_2O				
O(1W)−H(1A)···O(12a)	0.7900	2.0400	2.788(6)	157.00
O(1W)–H(1B)···O(44)	0.8100	1.8600	2.660(5)	169.00
O(2W)–H(2A)···O(41a)	0.8500	2.5600	3.108(5)	123.00
O(2W)–H(2A)···O(42a)	0.8500	1.8200	2.675(6)	179.00
O(2W)–H(2B)···O(14)	0.8000	1.9500	2.746(5)	170.00
O(3W)–H(3A)···O(5Wb)	0.8500	2.0900	2.941(16)	180.00
O(3W)–H(3B)···O(34c)	0.8500	1.9400	2.792(5)	180.00
O(4W)–H(4A)···O(2Wd)	0.9000	1.7700	2.675(5)	174.00
O(4W)–H(4B)···O(34d)	0.8500	2.0400	2.891(5)	180.00
O(5W)–H(5A)···O(1W)	0.8400	1.8300	2.655(7)	170.00
O(5W)–H(5B)···O(3W)	0.8000	2.0400	2.799(7)	157.00
O(6W)–H(6A)···O(42)	0.9400	2.1400	2.892(9)	136.00
O(6W)–H(6B)···O(23e)	0.9600	2.1300	3.077(9)	167.00
O(7W)–H(7A)···O(23)	0.9300	2.5600	3.232(10)	130.00
O(7W)–H(7A)···O(24)	0.9300	1.9600	2.882(10)	173.00
O(7W)–H(7B)···O(54B)	0.8100	2.5400	3.006(16)	118.00
O(7W)–H(7B)···O(6We)	0.8100	2.3100	3.115(17)	171.00
O(51)–H(51A)···O(21f)	0.8900	2.1600	2.994(4)	155.00
O(51)–H(51C)···N(41)	0.9500	2.3400	2.936(5)	120.00
O(51)–H(51C)···O(44g)	0.9500	2.1900	2.905(5)	131.00
O(52)–H(52A)···O(4W)	0.8800	1.9700	2.822(5)	162.00
O(52)–H(52B)···O(24h)	0.7600	1.9900	2.698(5)	155.00
O(53)–H(53A)···O(7W)	0.7500	2.0100	2.734(8)	163.00
O(53)–H(53B)···O(3W)	0.7400	2.0500	2.786(5)	171.00
O(54A)–H(54A)···O(6We)	0.6000	1.8900	2.139(13)	106.00
O(54A)–H(54B)···O(4W)	0.7200	2.2000	2.854(11)	153.00
O(54A)–H(54B)···O(41)	0.7200	2.3600	2.755(13)	117.00
O(54A)–H(54D)···O(4W)	1.0300	1.9500	2.854(11)	146.00
O(54A)–H(54D)···O(52)	1.0300	2.4600	3.270(11)	135.00
Pr-Hpda-H_2O				
O(9)–H(7)···O(11a)	0.921(13)	1.841(13)	2.761(3)	177.1(13)
O(11)–H(9)···O(1b)	0.91(3)	2.04(3)	2.930(3)	167(3)
O(10)–H(10)···O(3b)	0.92(3)	1.90(4)	2.732(4)	149(3)
O(10)–H(11)···O(8c)	0.91(3)	1.84(3)	2.737(4)	168(3)
O(13)–H(12)···O(14)	0.92(3)	2.05(3)	2.829(6)	141(4)
O(14)–H(13)···O(7)	0.93(4)	2.27(12)	2.968(5)	131(11)
O(14)–H(13)···O(9)	0.93(4)	2.59(7)	3.360(5)	140(9)
O(12)–H(14)···O(2d)	0.92(3)	1.80(3)	2.714(4)	172(3)
O(11)–H(15)···O(2e)	0.92(4)	1.98(4)	2.886(3)	165(3)
O(13)–H(16)···O(8)	0.93(2)	1.76(3)	2.669(4)	167(4)

O(12)–H(17)···O(11f)	0.924(17)	2.05(2)	2.913(3)	154(4)
O(9)–H(18)···O(12g)	0.93(3)	1.84(3)	2.730(4)	161(2)
O(6)–H(19)···O(13h)	0.94(4)	1.57(4)	2.495(4)	172(4)
		Pr-pda-H_2O		
O(1W)–H(1WA)···O(1Wa)	0.8500	2.2100	2.518(17)	101.00
O(1)–H(1A)···O(1W)	0.8500	2.4000	2.960(14)	124.00
O(1)–H(1B)···O(13b)	0.8500	2.5500	2.902(3)	106.00
O(2)–H(2A)···O(14c)	0.8500	2.2300	2.809(3)	126.00
O(3)–H(3A)···O(1d)	0.8500	2.3000	3.091(3)	154.00
O(3)–H(3B)···O(6e)	0.8500	2.5800	2.921(3)	105.00
O(3)–H(3B)···O(7e)	0.8500	2.0900	2.860(3)	150.00
O(10)–H(10A)···O(15f)	0.8200	2.5900	3.205(3)	133.00
O(10)–H(10A)···N(1f)	0.8200	2.1500	2.931(3)	159.00
O(14)–H(14)···O(2d)	0.8200	2.0700	2.809(3)	150.00

Symmetry codes: a) 1+*x*, 1+*y*, *z*; b) 1−*x*, 2−*y*, −*z*; c)1−*x*, 1−*y*, −*z*; d) −1+*x*, *y*, *z*; e) −*x*, 1−*y*, 1−*z*; f) *x*, 1+*y*, *z*; g) 1−*x*, 2−*y*, 1−*z*; h) −*x*, 1−*y*, −*z*; i) *x*, −1+*y*, −1+*z*; for **Pr-Ce-H_2pda-H_2O;** a) *x*, *y*, 1+*z*; b) *x*, 1/2−*y*, −1/2+*z*; c) 1−*x*, −1/2+*y*, 3/2−*z*; d) 1−*x*, 1/2+*y*, 3/2−*z*; e) 2−*x*, −*y*, 1−*z*; f) 1−*x*, 1−*y*, 1−*z*; g) 1−*x*, −1/2+*y*, 3/2−*z*; h) *x*, −1+*y*, *z*; for **Pr-Hpda-H_2O;** a) −*x*, −*y*, 1−*z*; b) −1+*x*, *y*, *z*; c)1− *x*, −1/2+*y*, 1/2−*z*; d)1− *x*, 1/2+*y*, 1/2−*z*; e) 1−*x*, 1−*y*,1− *z*; f) 2−*x*, 1−*y*, 1−*z*; for **Pr-pda-H_2O**.

II. Purification of Pr-Hpda-H_2O

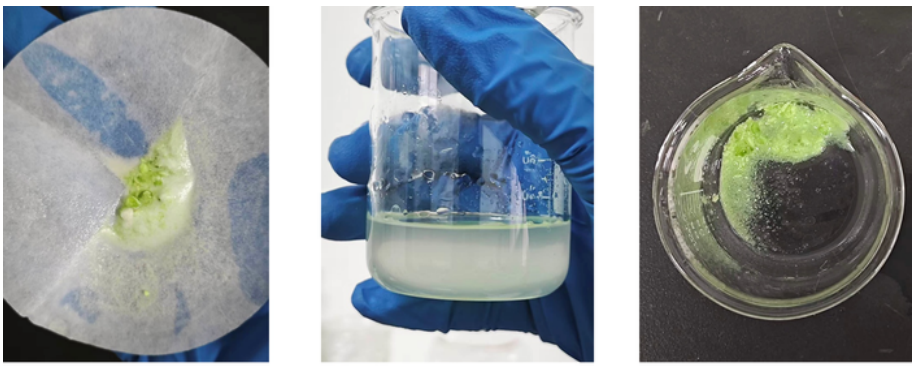

Fig. S1 Photographs showing the DMF-assisted purification process of **Pr-Hpda-H_2O**: (a) crude product containing green crystals and a white powdery by-product; (b) phase separation after addition of DMF, with the white by-product dispersed in the liquid phase and the green crystals settled at the bottom; (c) purified green crystals after decantation and removal of the white by-product.

The DMF washing step was used solely as a purification procedure for Pr-Hpda-H_2O because its crude product contained the target green crystals together with a white powdery by-product. As shown in Fig. S1a–c, the crude product consisted of both green crystals and a white powder. Upon addition of DMF, the white by-product became dispersed in the liquid phase, whereas the denser green crystals settled at the bottom of the vessel, allowing the impurity to be removed by decantation. By contrast, this white by-product was not observed for the other two compounds, and therefore no DMF washing step was required for their purification. In addition, because this material is not an open-porous framework, any possible residual DMF would more likely arise from surface adsorption rather than pore confinement.

III. Characterization: PXRD patterns

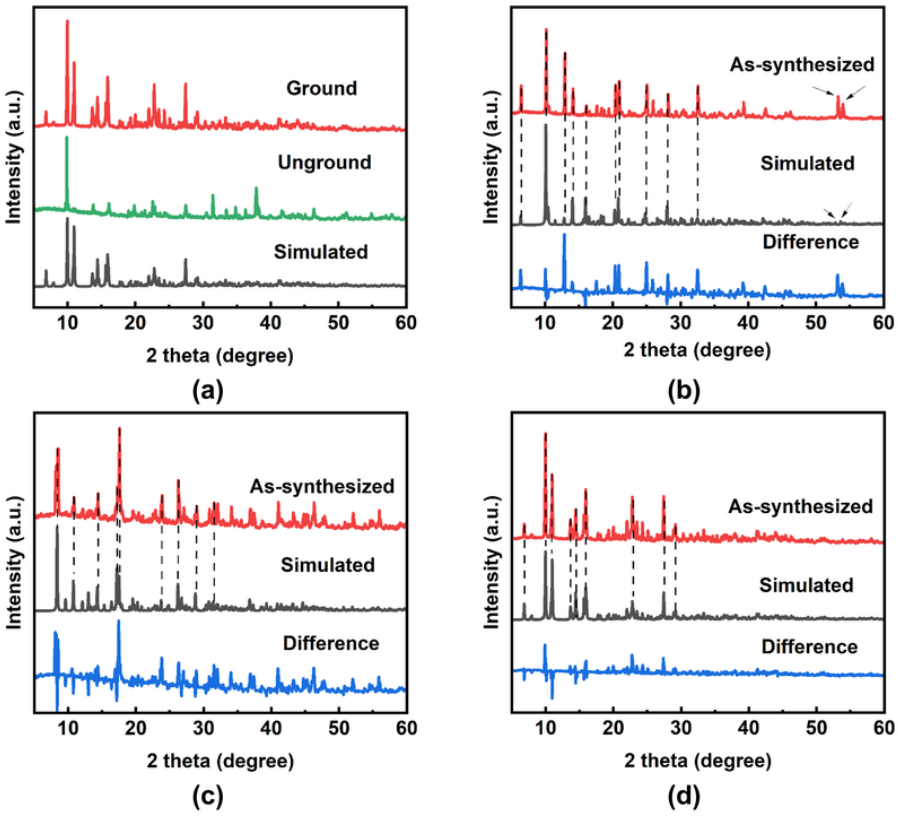

Fig. S2 Comparison of the experimental and simulated PXRD patterns. Comparison of the PXRD patterns of simulated, ground, and unground crystalline **Pr-Ce-H_2pda-H_2O** samples (a). Experimental, simulated, and normalized difference plots of **Pr-Hpda-H_2O** (b), **Pr-pda-H_2O** (c), and **Pr-Ce-H_2pda-H_2O** (d). Several major reflections are marked by dashed guide lines to facilitate visual comparison of peak positions.

It should be noted that incomplete agreement in relative peak intensities between experimental PXRD patterns and ideal simulated patterns is common in powder diffraction. According to the PXRD literature, the observed intensities in powder patterns are influenced not only by the crystal structure itself, but also by diffraction geometry, sample preparation, and specimen-related factors.[4] Therefore, differences in relative peak intensities between the experimental and simulated patterns do not necessarily indicate the presence of impurity phases.

To further illustrate this point, we measured the PXRD pattern of an unground crystalline sample of Pr-Ce-H_2pda-H_2O (Fig. S2a). The result shows that, without grinding, although some reflections are strong, the overall pattern is incomplete. This indicates that the sample state and preferred orientation can significantly affect the experimental PXRD pattern. Accordingly, grinding is usually necessary to obtain a more representative powder pattern. In addition, the literature shows that crystallite size

and lattice strain can affect Bragg peaks and may lead to changes in peak width, peak intensity, and 2θ position.[5] Another study has further shown that peak shift and peak broadening can occur together with increased strain and reduced crystallite size.[6] Therefore, the differences in local peak profile, peak width, and a few peak positions between the experimental and simulated patterns can be reasonably attributed to changes in crystallite size and lattice strain caused by sample grinding. Furthermore, previous studies have shown that the standard deviation in peak-position determination is closely related to the intensity-to-background ratio. As a result, weaker reflections generally have greater positional uncertainty.[7] Although the unground-sample test was carried out for Pr-Ce-H_2pda-H_2O, it illustrates how sample state and preferred orientation can significantly affect the experimental PXRD patterns in this family of compounds.

To facilitate visual comparison between the experimental and simulated patterns, normalized difference plots were calculated for all three compounds (Fig. S2b–d). Several strong main reflections were marked with vertical guide lines to make the comparison of peak positions clearer. In addition, the calculated and experimental positions of several selected major reflections were listed for all three compounds (Table S4–S6). These supplementary comparisons show that the experimental and simulated patterns remain generally consistent in the positions of the major reflections, while the main differences are found in relative intensities, local peak profiles, and slight peak-position shifts. Notably, the experimental PXRD patterns of Pr-Hpda-H_2O and Pr-pda-H_2O exhibit an overall shift of the major reflections toward higher 2θ values relative to the simulated patterns, particularly in the high-angle region. This feature may reasonably be attributed to grinding-related lattice strain, possibly accompanied by changes in crystallite size.

Based on the overall PXRD comparison, including the newly added difference plots and peak-position analysis, we consider that these differences are more likely caused by preferred orientation and grinding-related microstructural effects than by obvious impurity phases in the bulk. Moreover, our assessment of sample composition does not rely solely on PXRD. Although XPS is a surface-sensitive technique and cannot by itself exclude trace bulk impurities, it did not reveal any obvious anomalous signals attributable to impurity components (Fig. S6) and is therefore consistent with the PXRD-based interpretation.

Taken together, the current results support the conclusion that the obtained samples

are predominantly composed of the target crystalline phases, while the observed differences are more likely attributable to powder-sample preparation, preferred orientation, and grinding-related microstructural effects rather than to obvious impurity phases.

Table S4 Comparison of selected major PXRD peak positions between the calculated and experimental patterns of **Pr-Ce-H_2pda-H_2O**.

Calculated	Experimental	Deviation
6.82	6.82	0.00
9.96	9.96	0.00
10.96	10.98	0.00
13.66	13.66	0.00
14.42	14.42	0.00
15.92	15.92	0.00
22.78	22.78	0.00
27.42	27.42	0.00
29.16	29.18	+0.02

Table S5 Comparison of selected major PXRD peak positions between the calculated and experimental patterns of **Pr-Hpda-H_2O**.

Calculated	Experimental	Deviation
6.40	6.40	0.00
10.10	10.10	0.00
12.80	12.84	+0.04
14.04	14.05	+0.01
15.96	16.00	+0.04
20.28	20.32	+0.04
24.90	24.96	+0.06
28.00	28.10	+0.1
32.40	32.48	+0.08
52.88	53.18	+0.3
53.66	53.88	+0.22

Table S6 Comparison of selected major PXRD peak positions between the calculated and experimental patterns of **Pr-pda-H_2O**.

Calculated	Experimental	Deviation
8.36	8.4	+0.04
10.78	10.8	+0.02
14.28	14.34	+0.06
17.22	17.24	+0.02
17.5	17.5	0.00
23.72	23.78	+0.06
26.2	26.2	0.00
28.78	28.88	+0.10
31.94	32.02	+0.08

IV. Characterization: FT-IR spectra

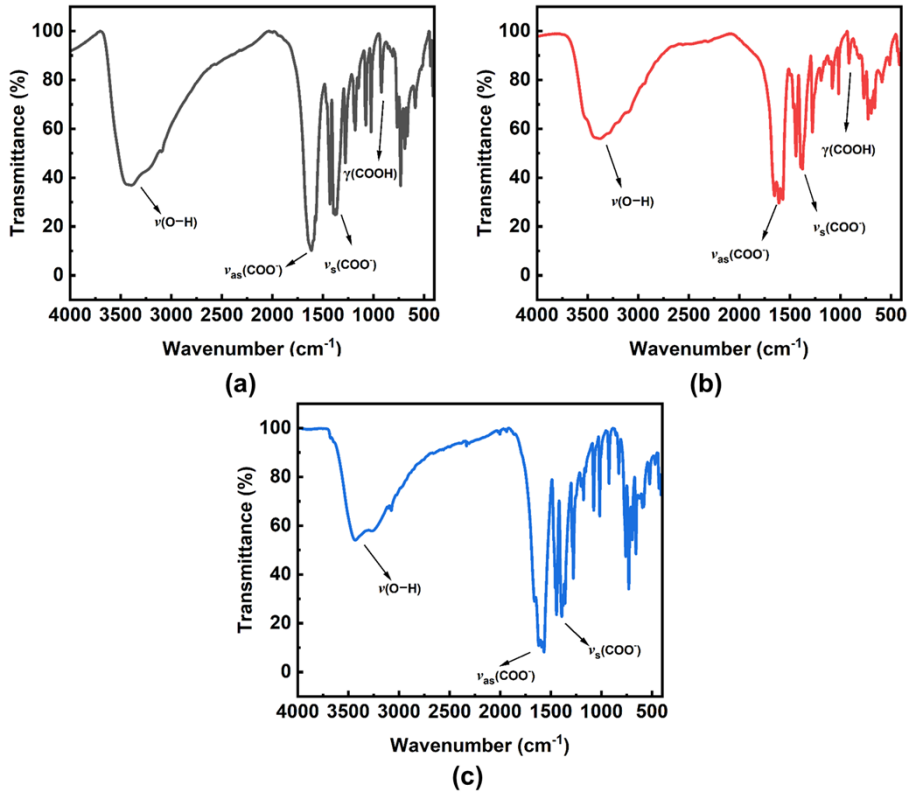

Fig. S3 FT-IR spectra of **Pr-Ce-H_2pda-H_2O** (a), **Pr-Hpda-H_2O** (b), and **Pr-pda-H_2O** (c) recorded in the solid state at room temperature over the range of 4000–400 cm^{-1}.[8]

V. Characterization: FT-IR spectra and TG-MS analysis

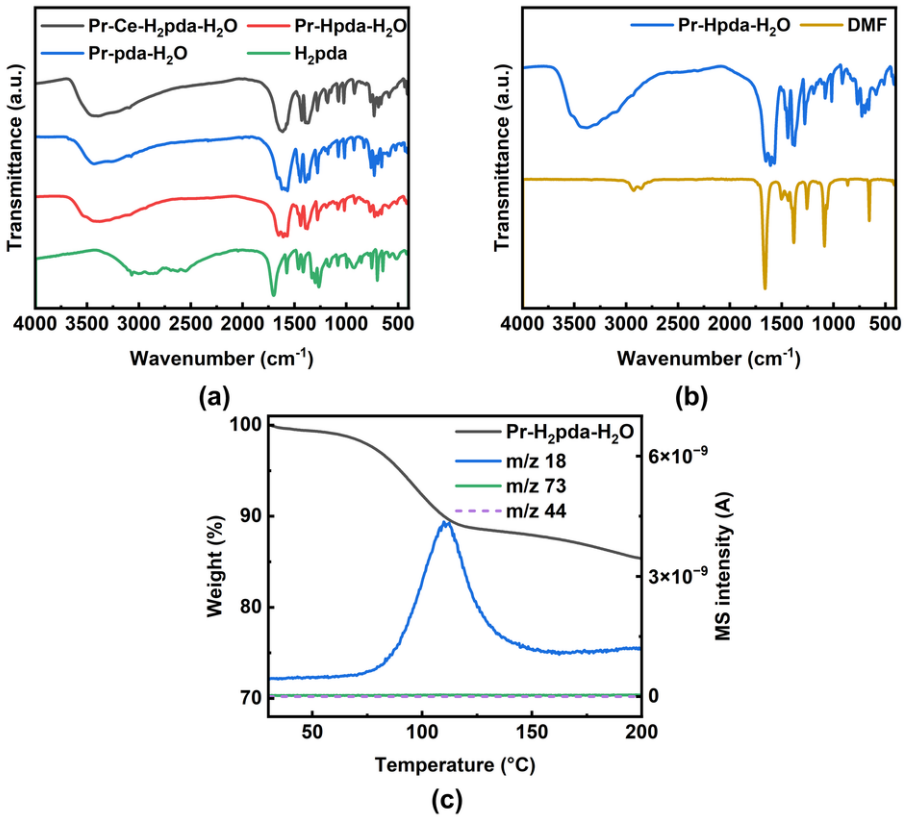

Fig. S4 FT-IR and TG-MS evidence related to the purification of **Pr-Hpda-H_2O** and the verification of residual solvent removal. (a) FT-IR spectra of **Pr-Ce-H_2pda-H_2O**, **Pr-Hpda-H_2O**, **Pr-pda-H_2O**, and H_2pda; (b) comparison of the FT-IR spectra of purified **Pr-Hpda-H_2O** and liquid DMF; (c) TG-MS profile of purified **Pr-Hpda-H_2O**, showing the TG curve together with selected extracted-ion traces (m/z 18, 73, and 44). In the main low-temperature mass-loss region, the dominant evolved species is H_2O (m/z 18), while no obvious increase in DMF-related signals is observed.

We examined the FT-IR spectra of Pr-Ce-H_2pda-H_2O, Pr-Hpda-H_2O, and Pr-pda-H_2O together with that of the organic ligand H_2pda. As shown in Fig. S4a, the three compounds exhibit fingerprint features similar to those of H_2pda, consistent with coordination of the ligand to the rare-earth ions and formation of the target products. In addition, Fig. S4b compares the FT-IR spectrum of purified Pr-Hpda-H_2O with that of liquid DMF. Pure DMF shows a strong characteristic carbonyl stretching band near 1670 cm^{-1}. However, because partial overlap between the IR bands of DMF and those of Pr-Hpda-H_2O cannot be completely excluded, we considered that FT-IR evidence alone might not be sufficient to fully resolve the residual DMF.

Therefore, we further performed thermogravimetry-mass spectrometry (TG-MS)

analysis on the purified bulk sample of Pr-Hpda-H_2O to identify the evolved species during heating (Fig. S4c). In this analysis, m/z 18, 73, and 44 were monitored, where m/z 18 corresponds to H_2O, m/z 73 corresponds to the molecular ion of DMF, and m/z 44 corresponds to a characteristic fragment ion arising from DMF thermal decomposition according to reported mass-spectral fragmentation data.[9] The results show that the dominant signal in the main low-temperature mass-loss region is m/z 18, whereas the DMF-related signals (m/z 73 and m/z 44) remain close to the baseline and do not show a synchronous increase with the major mass-loss event. These observations indicate that the mass-loss process at low temperatures (below 200 °C) is mainly associated with the release of water species rather than residual DMF.

Taken together, the purification photographs and the TG-MS results consistently support the conclusion that DMF was used only as a purification medium for Pr-Hpda-H_2O and that no obvious residual DMF remained in the purified bulk sample.

VI. Characterization: XPS survey

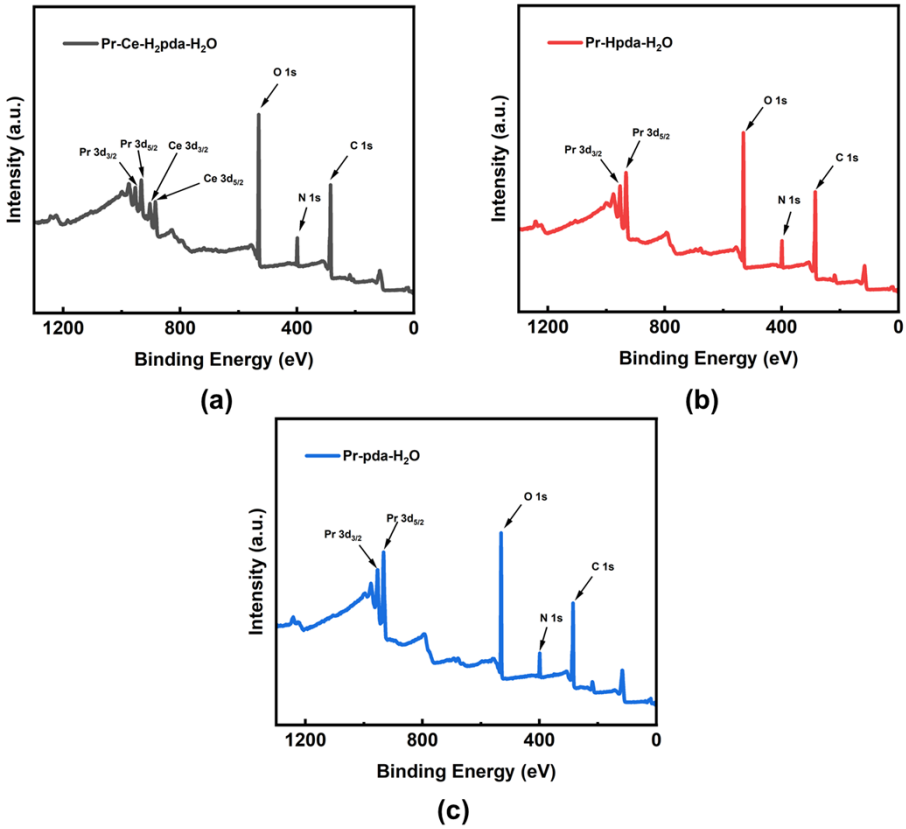

Fig. S5 XPS survey spectra of **Pr-Ce-H_2pda-H_2O** (a), **Pr-Hpda-H_2O** (b) and **Pr-pda-H_2O** (c).

VII. Characterization: High-resolution XPS spectra

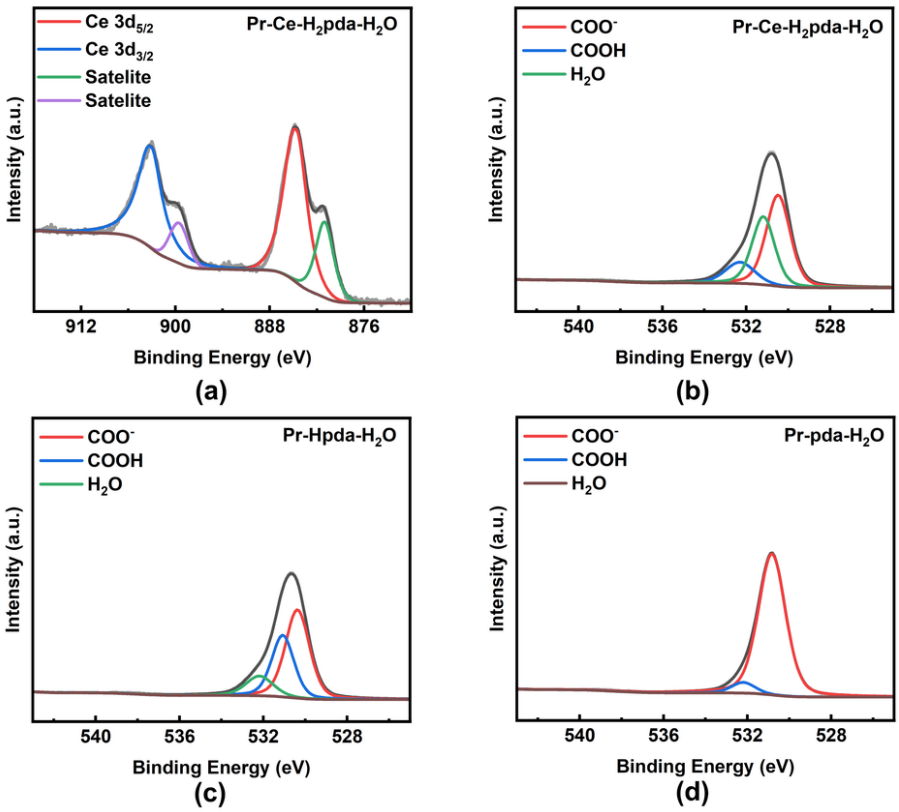

Fig. S6 High-resolution XPS spectra of the prepared compounds. (a) Ce 3d spectrum of **Pr-Ce-H$_2$pda-H$_2$O**; (b) O 1s spectrum of **Pr-Ce-H$_2$pda-H$_2$O**; (c) O 1s spectrum of **Pr-Hpda-H$_2$O**; (d) O 1s spectrum of **Pr-pda-H$_2$O**.

VIII. Stability: TGA curves

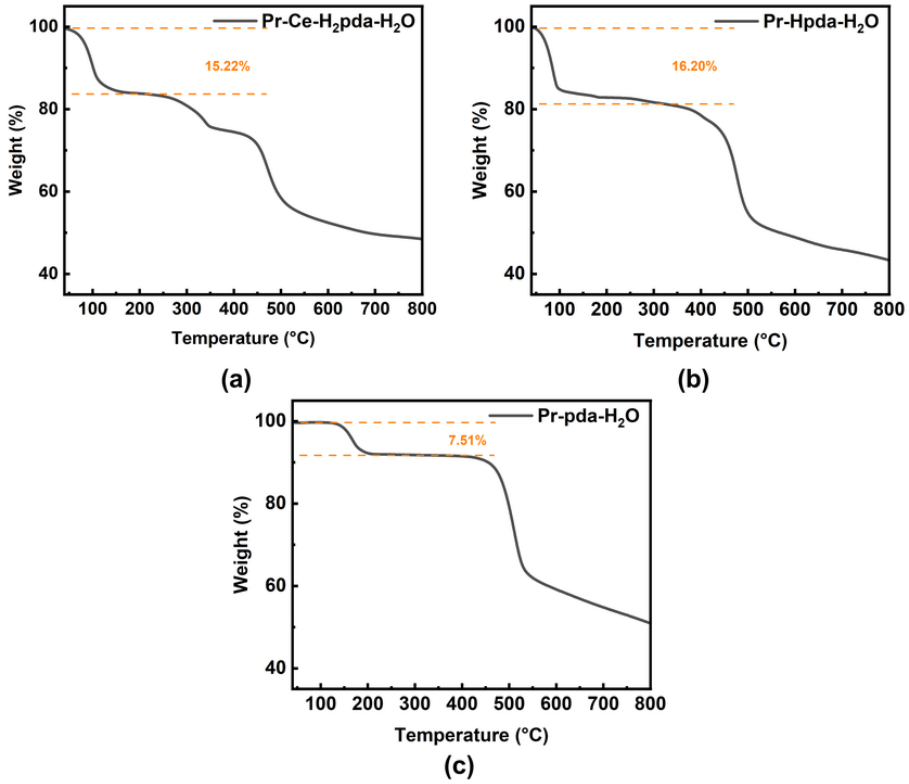

Fig. S7 Thermogravimetric curves of **Pr-Ce-H_2pda-H_2O** (a), **Pr-Hpda-H_2O** (b) and **Pr-pda-H_2O** (c).

IX. Characterization: SEM images

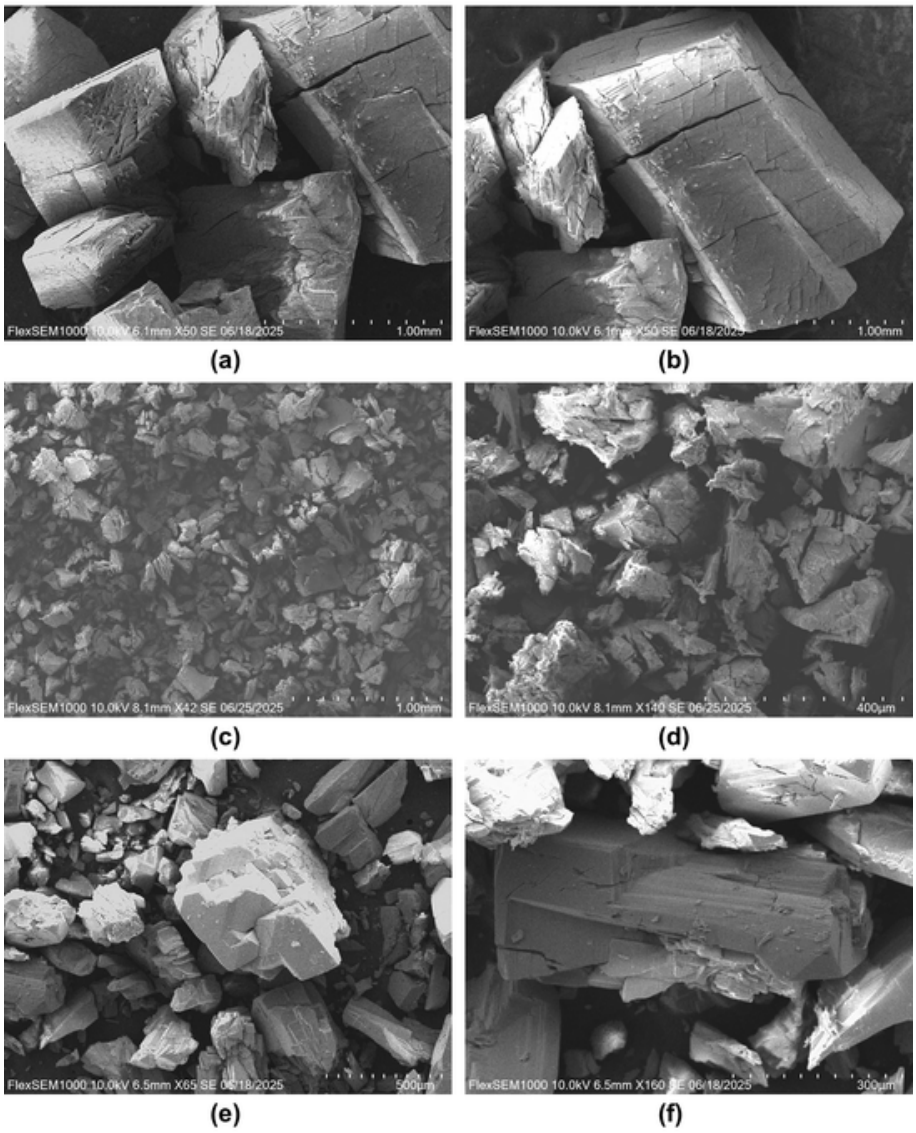

Fig. S8 SEM images showing full-view (a) and magnified-view (b) morphologies of **Pr-Ce-H_2pda-H_2O**; full-view (c) and magnified-view (d) morphologies of **Pr-Hpda-H_2O**; and full-view (e) and magnified-view (f) morphologies of **Pr-pda-H_2O**.

X. Comparison of chemical stability

Table S7 Comparison of chemical stability of **Pr-Ce-H_2pda-H_2O**, **Pr-Hpda-H_2O** and **Pr-pda-H_2O** with previously reported MOF materials

Materials	pH range	Time (day or hour)	References
Pr-Ce-H_2pda-H_2O	3–11	12 hours	This work
Pr-Hpda-H_2O	3–11	12 hours	This work
Pr-pda-H_2O	3–11	12 hours	This work
PCN-777	3–11	12 hours	[10]
$[Cu_3(\mu_3\text{-}OH)(H_2O)_3(atz)_3]$ $[P_2W_{18}O_{62}]\cdot 14H_2O$ [a]	2–12	20 hours	[11]
oCB-MOF-1	2–12	15 hours	[12]
USTC-8(In)	0–11	12 hours	[13]
PCN-225	1–11	12 hours	[14]
PCN-333(Al)	3–9	Overnight	[15]
PCN-333(Fe)	3–9	Overnight	[15]
MIL-53(Cr)	1–12	6 hours	[16]
UiO-67	4–9	2 hours	[17]
H-UiO-66–3.8 nm	2–8	2 hours	[18]
H-UiO-66–17.3 nm	2–8	2 hours	[18]
ZIF-8	5–10	5 hours	[19]
MIL-101	4–5	12 hours	[20]
Co-2PPA [b]	3–11	12 hours	[21]
Co-4PPA [b]	3–11	12 hours	[21]

[a] Hatz = 3-amino-1,2,4-triazolate. [b] PPA = 4-(3-pyridinyl)-2-amino pyrimidine.

XI. Electrochemical measurements

Experimental details of proton conductivity measurements:

For the proton conductivity measurements, the pelletized sample was placed in a sealed glass vessel, and the relative humidity inside the chamber was controlled using saturated salt solutions placed at the bottom of the vessel, including K_2SO_4 (~97% RH), NaCl (~75% RH), $NaNO_2$ (~65% RH), and $Mg(NO_3)_2$ (~53% RH). The vessel was sealed with a modified stopper equipped with a thermometer port and wire grooves to maintain a closed high-humidity environment during the measurements. Temperature control was achieved by immersing the entire sealed vessel in a thermostatic water bath, while the internal temperature was monitored directly with a thermometer. Before the impedance measurements, the assembled setup was heated to 60 °C and maintained for 1 h, and then allowed to stand overnight to ensure sufficient hydration equilibrium under the selected humidity condition. During the variable-temperature AC impedance measurements, the system was first heated to the preset maximum temperature and allowed to equilibrate. At each temperature, the measurement was continued until the resistance value no longer showed any obvious change, which was taken to indicate that equilibrium had been reached. The impedance spectra were then continuously collected during the natural cooling process in order to minimize possible temperature gradients between the sample and the humid environment.

Equivalent circuit model:

- R(RQ)(RQ)W:

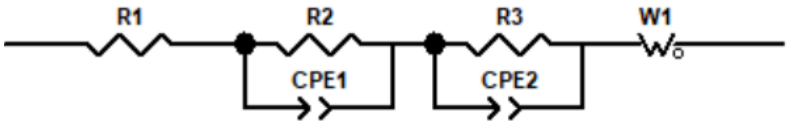

Scheme S1. The equivalent circuit (R1(R2CPE1)(R3CPE2)W1), in which R1 is bulk resistor, CPE1 and R2 are constant phase element and resistor for grain boundary, CPE2 and R3 are constant phase element and resistor for interface contact, W1 is Warburg diffusion element.

- R(RQ)(RQ):

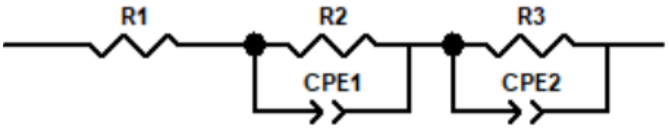

Scheme S2. The equivalent circuit (R1(R2CPE1)(R3CPE2)), in which R1 is bulk resistor, CPE1 and R2 are constant phase element and resistor for grain boundary, CPE2 and R3 are constant phase element and resistor for interface contact.

- R(RQ):

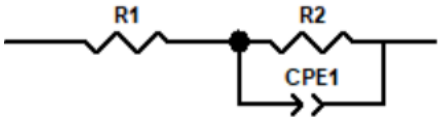

Scheme S3. The equivalent circuit (R1(R2CPE1)), in which R1 is bulk resistor, CPE1 and R2 are constant phase element and resistor for grain boundary.

Table S8 Fitted results of **Pr-Ce-H_2pda-H_2O**

Conditions	Equivalent Circuit	χ^2
298 K and ~53% RH	(R1(R2CPE1))	5.86×10^{-5}
298 K and ~65%RH	(R1(R2CPE1))	2.53×10^{-4}
298 K and ~75%RH	(R1(R2CPE1)(R3CPE2))	5.51×10^{-4}
298 K and ~97%RH	(R1(R2CPE1)(R3CPE2)W1)	3.89×10^{-4}
303 K and ~97%RH	(R1(R2CPE1)(R3CPE2)W1)	1.80×10^{-4}
308 K and ~97%RH	(R1(R2CPE1)(R3CPE2)W1)	4.24×10^{-4}
313 K and ~97%RH	(R1(R2CPE1)(R3CPE2)W1)	2.34×10^{-4}
318 K and ~97%RH	(R1(R2CPE1)(R3CPE2)W1)	2.81×10^{-4}
323 K and ~97%RH	(R1(R2CPE1)(R3CPE2)W1)	4.13×10^{-4}
328 K and ~97%RH	(R1(R2CPE1)(R3CPE2)W1)	2.75×10^{-4}
333 K and ~97%RH	(R1(R2CPE1)(R3CPE2)W1)	5.10×10^{-4}
338 K and ~97%RH	(R1(R2CPE1)(R3CPE2)W1)	1.23×10^{-4}
343 K and ~97%RH	(R1(R2CPE1)(R3CPE2)W1)	2.47×10^{-4}
348 K and ~97%RH	(R1(R2CPE1)(R3CPE2)W1)	2.52×10^{-4}
353 K and ~97%RH	(R1(R2CPE1)(R3CPE2)W1)	4.97×10^{-4}
0 h (298 K and ~97% RH)	(R1(R2CPE1)(R3CPE2)W1)	3.89×10^{-4}
1 h (298 K and ~97% RH)	(R1(R2CPE1)(R3CPE2)W1)	6.91×10^{-4}
2 h (298 K and ~97% RH)	(R1(R2CPE1)(R3CPE2)W1)	5.16×10^{-4}
3 h (298 K and ~97% RH)	(R1(R2CPE1)(R3CPE2)W1)	3.30×10^{-4}
4 h (298 K and ~97% RH)	(R1(R2CPE1)(R3CPE2)W1)	3.21×10^{-4}
5 h (298 K and ~97% RH)	(R1(R2CPE1)(R3CPE2)W1)	4.05×10^{-4}
6 h (298 K and ~97% RH)	(R1(R2CPE1)(R3CPE2)W1)	2.35×10^{-4}
7 h (298 K and ~97% RH)	(R1(R2CPE1)(R3CPE2)W1)	6.51×10^{-4}
8 h (298 K and ~97% RH)	(R1(R2CPE1)(R3CPE2)W1)	6.30×10^{-4}

Table S9 Fitted results of **Pr-Hpda-H_2O**

Conditions	Equivalent Circuit	χ^2
298 K and ~53% RH	(R1(R2CPE1))	7.89×10^{-3}
298 K and ~65%RH	(R1(R2CPE1))	6.88×10^{-3}
298 K and ~75%RH	(R1(R2CPE1)(R3CPE2))	1.68×10^{-3}
288 K and ~97%RH	(R1(R2CPE1)(R3CPE2))	1.05×10^{-3}
290 K and ~97%RH	(R1(R2CPE1)(R3CPE2))	6.98×10^{-4}
292 K and ~97%RH	(R1(R2CPE1)(R3CPE2))	6.43×10^{-4}
294 K and ~97%RH	(R1(R2CPE1)(R3CPE2))	9.69×10^{-3}
296 K and ~97%RH	(R1(R2CPE1)(R3CPE2))	7.59×10^{-3}
298 K and ~97%RH	(R1(R2CPE1)(R3CPE2))	1.11×10^{-3}
303 K and ~97%RH	(R1(R2CPE1)(R3CPE2))	7.94×10^{-4}
308 K and ~97%RH	(R1(R2CPE1)(R3CPE2))	1.02×10^{-3}
313 K and ~97%RH	(R1(R2CPE1)(R3CPE2))	6.26×10^{-4}
318 K and ~97%RH	(R1(R2CPE1)(R3CPE2))	7.21×10^{-4}
323 K and ~97%RH	(R1(R2CPE1)(R3CPE2))	5.98×10^{-4}
328 K and ~97%RH	(R1(R2CPE1)(R3CPE2))	6.00×10^{-4}
333 K and ~97%RH	(R1(R2CPE1)(R3CPE2))	7.48×10^{-4}
338 K and ~97%RH	(R1(R2CPE1)(R3CPE2))	6.03×10^{-4}
343 K and ~97%RH	(R1(R2CPE1)(R3CPE2))	5.57×10^{-4}
348 K and ~97%RH	(R1(R2CPE1)(R3CPE2))	4.42×10^{-4}
353 K and ~97%RH	(R1(R2CPE1)(R3CPE2))	6.24×10^{-4}
0 h (298 K and ~97% RH)	(R1(R2CPE1)(R3CPE2))	1.24×10^{-3}
1 h (298 K and ~97% RH)	(R1(R2CPE1)(R3CPE2))	8.31×10^{-4}
2 h (298 K and ~97% RH)	(R1(R2CPE1)(R3CPE2))	1.04×10^{-3}
3 h (298 K and ~97% RH)	(R1(R2CPE1)(R3CPE2))	7.51×10^{-4}
4 h (298 K and ~97% RH)	(R1(R2CPE1)(R3CPE2))	8.18×10^{-4}
5 h (298 K and ~97% RH)	(R1(R2CPE1)(R3CPE2))	4.77×10^{-4}
6 h (298 K and ~97% RH)	(R1(R2CPE1)(R3CPE2))	7.81×10^{-4}
7 h (298 K and ~97% RH)	(R1(R2CPE1)(R3CPE2))	6.33×10^{-4}
8 h (298 K and ~97% RH)	(R1(R2CPE1)(R3CPE2))	7.84×10^{-4}

Table S10 Fitted results of **Pr-pda-H_2O**

Conditions	Equivalent Circuit	χ^2
298 K and ~53% RH	(R1(R2CPE1))	1.35×10^{-3}
298 K and ~65%RH	(R1(R2CPE1))	8.68×10^{-4}
298 K and ~75%RH	(R1(R2CPE1)(R3CPE2))	1.54×10^{-3}
298 K and ~97%RH	(R1(R2CPE1)(R3CPE2))	4.32×10^{-4}
303 K and ~97%RH	(R1(R2CPE1)(R3CPE2))	6.58×10^{-4}
308 K and ~97%RH	(R1(R2CPE1)(R3CPE2))	7.48×10^{-4}
313 K and ~97%RH	(R1(R2CPE1)(R3CPE2))	7.71×10^{-4}
318 K and ~97%RH	(R1(R2CPE1)(R3CPE2))	4.21×10^{-4}
323 K and ~97%RH	(R1(R2CPE1)(R3CPE2))	5.02×10^{-4}
328 K and ~97%RH	(R1(R2CPE1)(R3CPE2))	5.41×10^{-4}
333 K and ~97%RH	(R1(R2CPE1)(R3CPE2))	4.56×10^{-4}
338 K and ~97%RH	(R1(R2CPE1)(R3CPE2))	5.48×10^{-4}
343 K and ~97%RH	(R1(R2CPE1)(R3CPE2))	2.93×10^{-4}
348 K and ~97%RH	(R1(R2CPE1)(R3CPE2))	4.42×10^{-4}
353 K and ~97%RH	(R1(R2CPE1)(R3CPE2))	3.79×10^{-4}
0 h (298 K and ~97% RH)	(R1(R2CPE1)(R3CPE2))	4.32×10^{-4}
1 h (298 K and ~97% RH)	(R1(R2CPE1)(R3CPE2))	8.92×10^{-4}
2 h (298 K and ~97% RH)	(R1(R2CPE1)(R3CPE2))	6.60×10^{-4}
3 h (298 K and ~97% RH)	(R1(R2CPE1)(R3CPE2))	9.54×10^{-4}
4 h (298 K and ~97% RH)	(R1(R2CPE1)(R3CPE2))	9.33×10^{-4}
5 h (298 K and ~97% RH)	(R1(R2CPE1)(R3CPE2))	4.75×10^{-4}
6 h (298 K and ~97% RH)	(R1(R2CPE1)(R3CPE2))	7.40×10^{-4}
7 h (298 K and ~97% RH)	(R1(R2CPE1)(R3CPE2))	4.85×10^{-4}
8 h (298 K and ~97% RH)	(R1(R2CPE1)(R3CPE2))	6.36×10^{-4}

• **Nyquist plots**

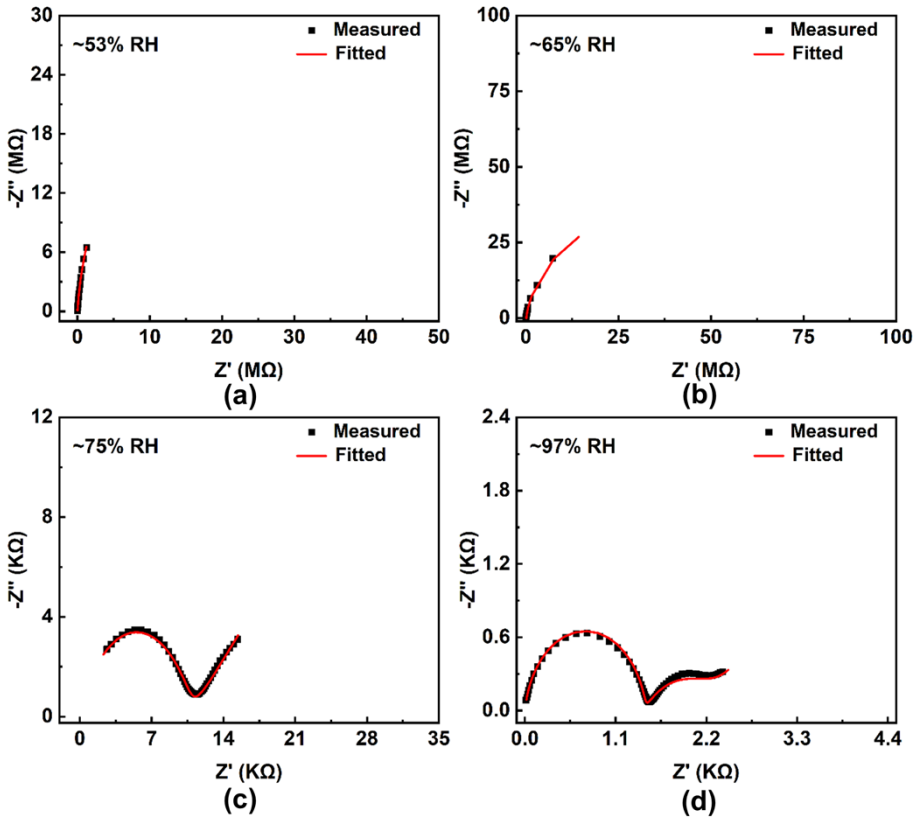

Fig. S9 Nyquist plots of **Pr-Ce-H_2pda-H_2O** recorded at 298 K under different relative humidities: 53% RH (a), 65% RH (b), 75% RH (c), and 97% RH (d).

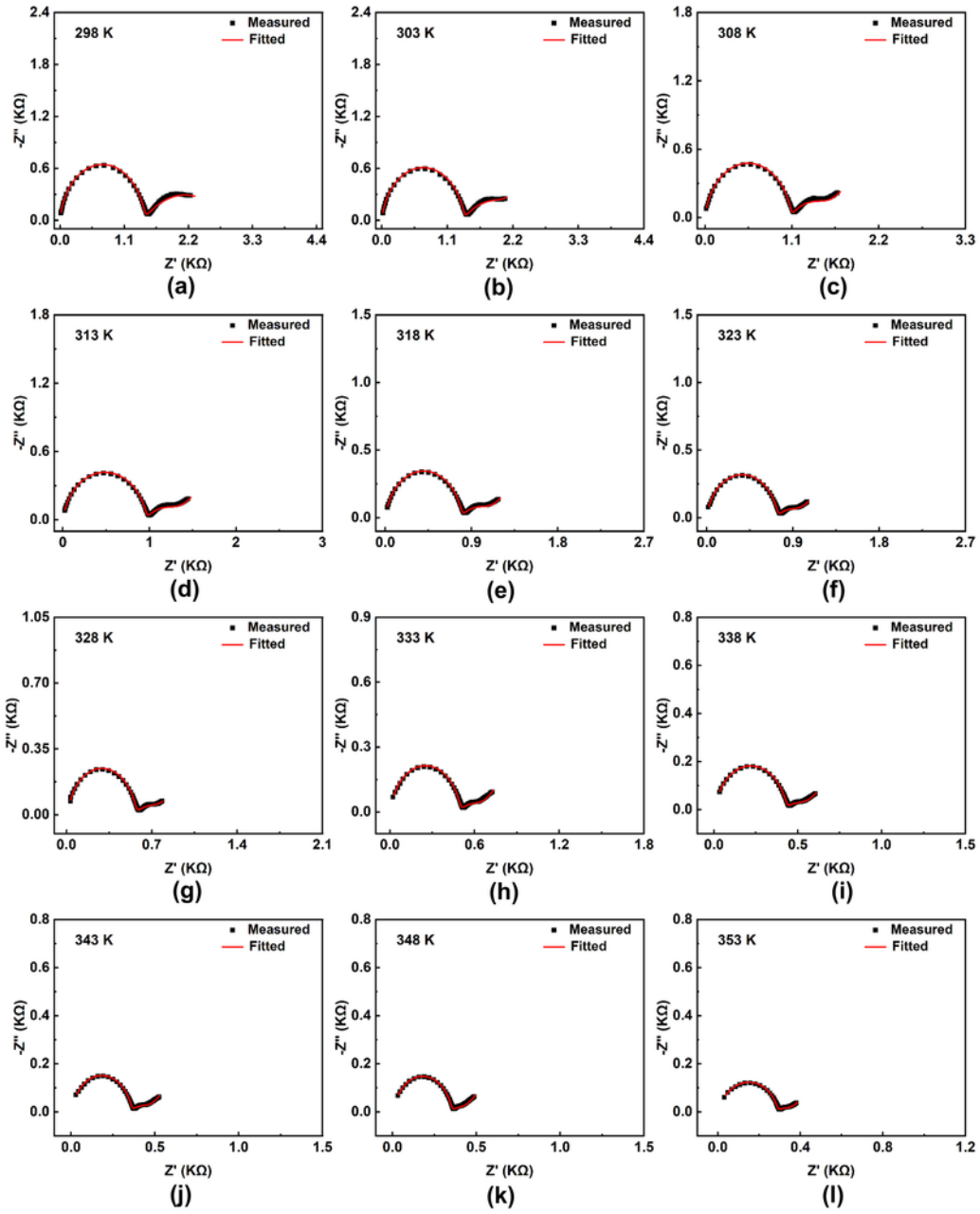

Fig. S10 Nyquist plots of **Pr-Ce-H_2pda-H_2O** measured at ~97% RH and temperatures of (a) 298 K, (b) 303 K, (c) 308 K, (d) 313 K, (e) 318 K, (f) 323 K, (g) 328 K, (h) 333 K, (i) 338 K, (j) 343 K, (k) 348 K, and (l) 353 K.

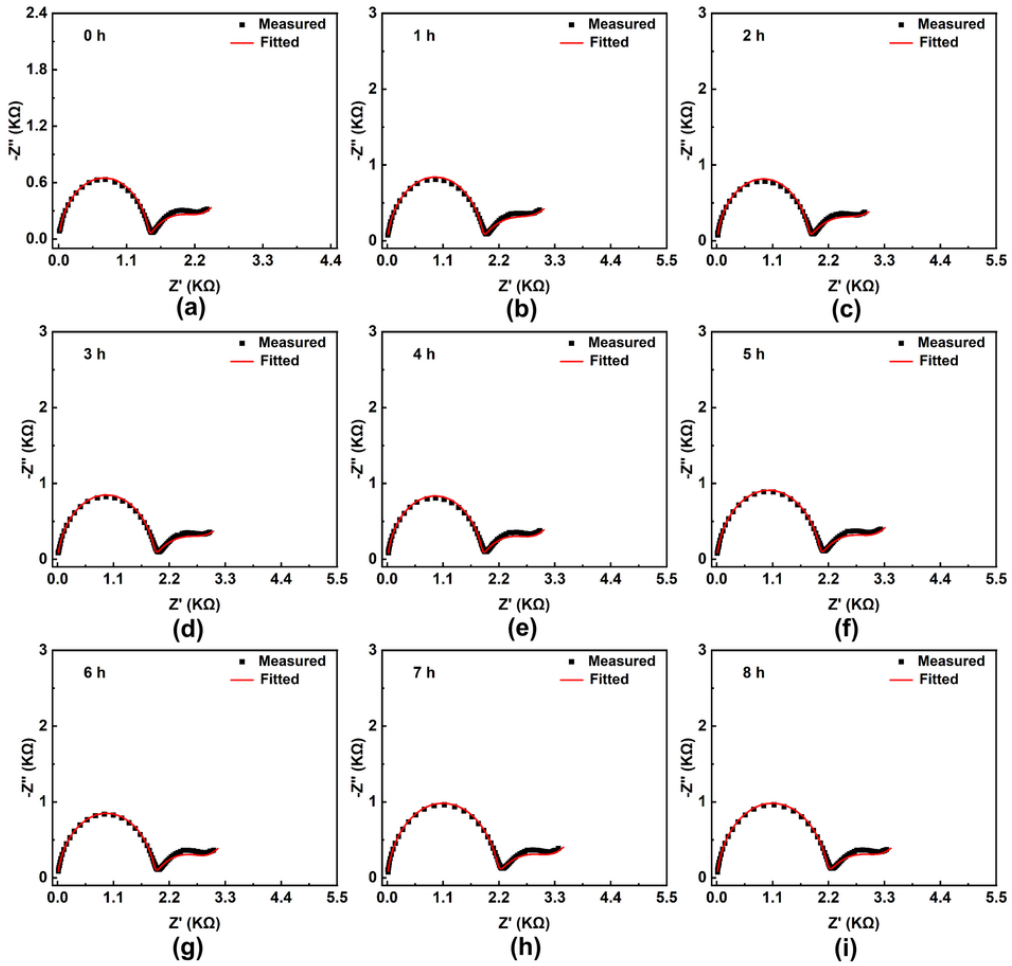

Fig. S11 Time-dependent Nyquist plots of **Pr-Ce-H_2pda-H_2O** recorded at 298 K and ~97% RH after different exposure times: 0 h (a), 1 h (b), 2 h (c), 3 h (d), 4 h (e), 5 h (f), 6 h (g), 7 h (h), and 8 h (i).

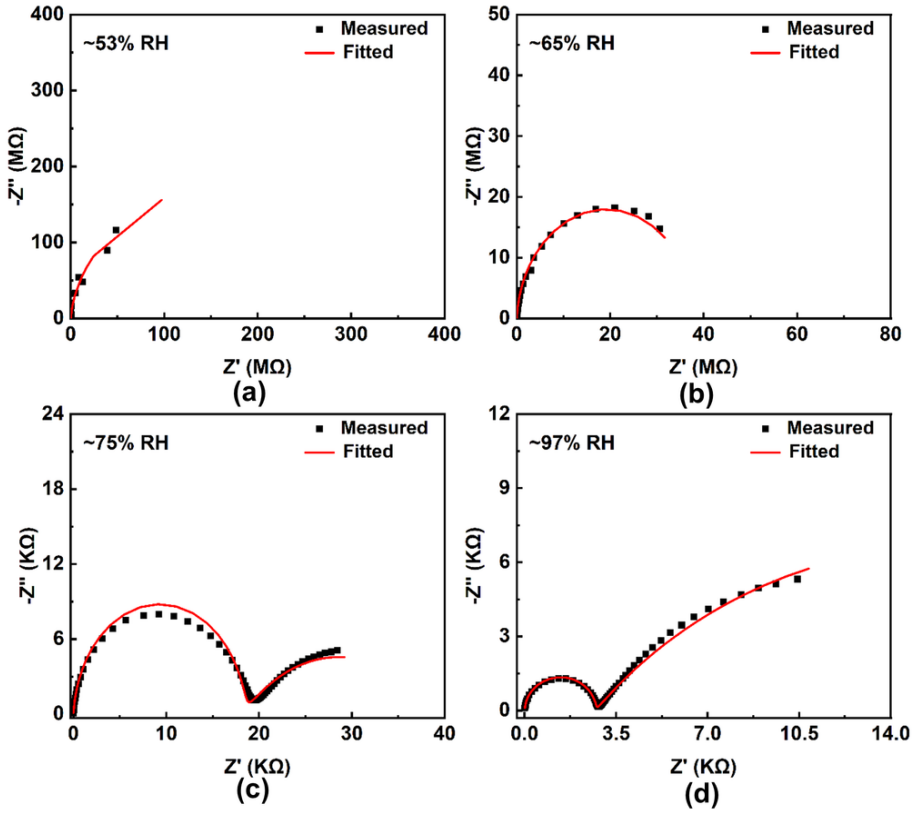

Fig. S12 Nyquist plots of **Pr-Hpda-H_2O** recorded at 298 K under different relative humidities: 53% RH (a), 65% RH (b), 75% RH (c), and 97% RH (d).

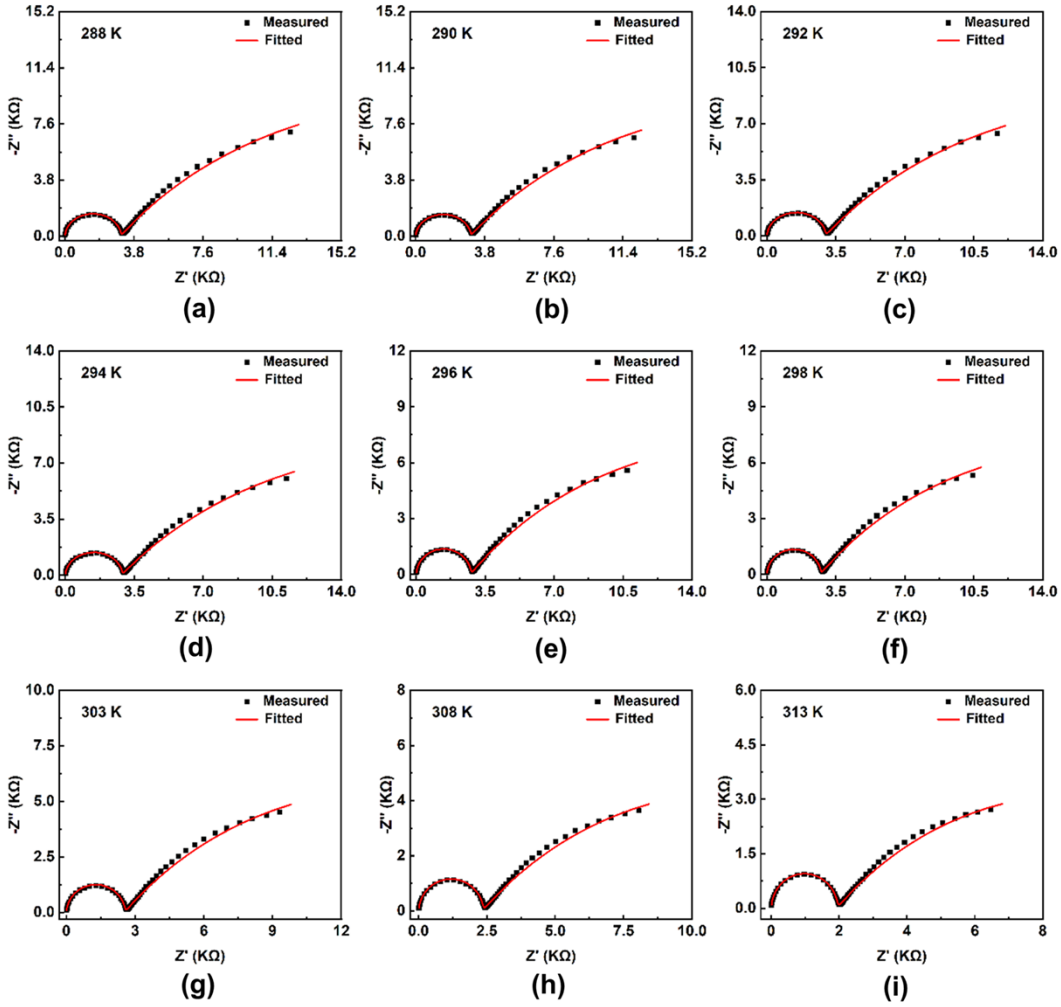

Fig. S13 Nyquist plots of **Pr-Hpda-H_2O** measured at ~97% RH and temperatures of 288 K(a), 290 K(b), 292 K(c), 294 K(d), 296 K(e), 298 K (f), 303 K (g), 308 K (h), 313 K (i).

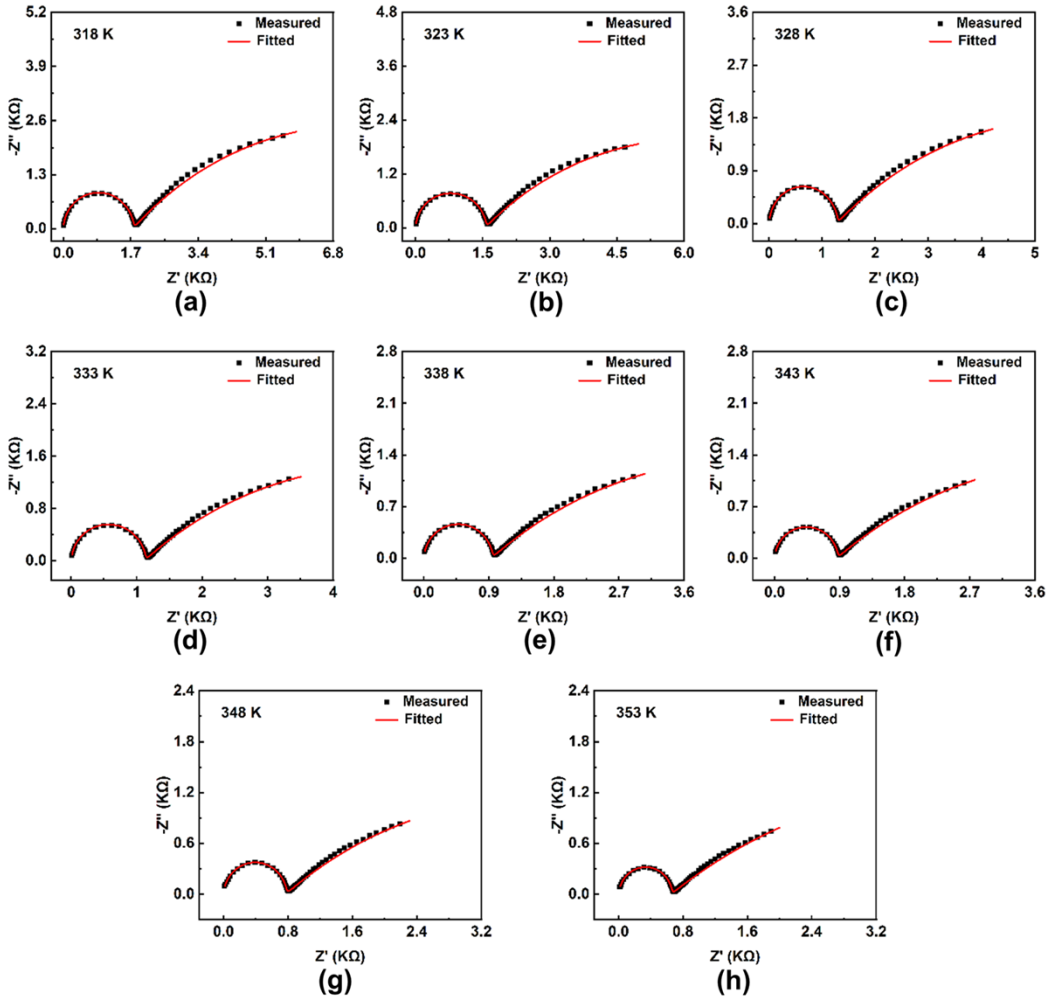

Fig. S14 Nyquist plots of **Pr-Hpda-H_2O** measured at ~97% RH and temperatures of 318 K (a), 323 K (b), 328 K (c), 333 K (d), 338 K (e), 343 K (f), 348 K (g) and 353 K (h).

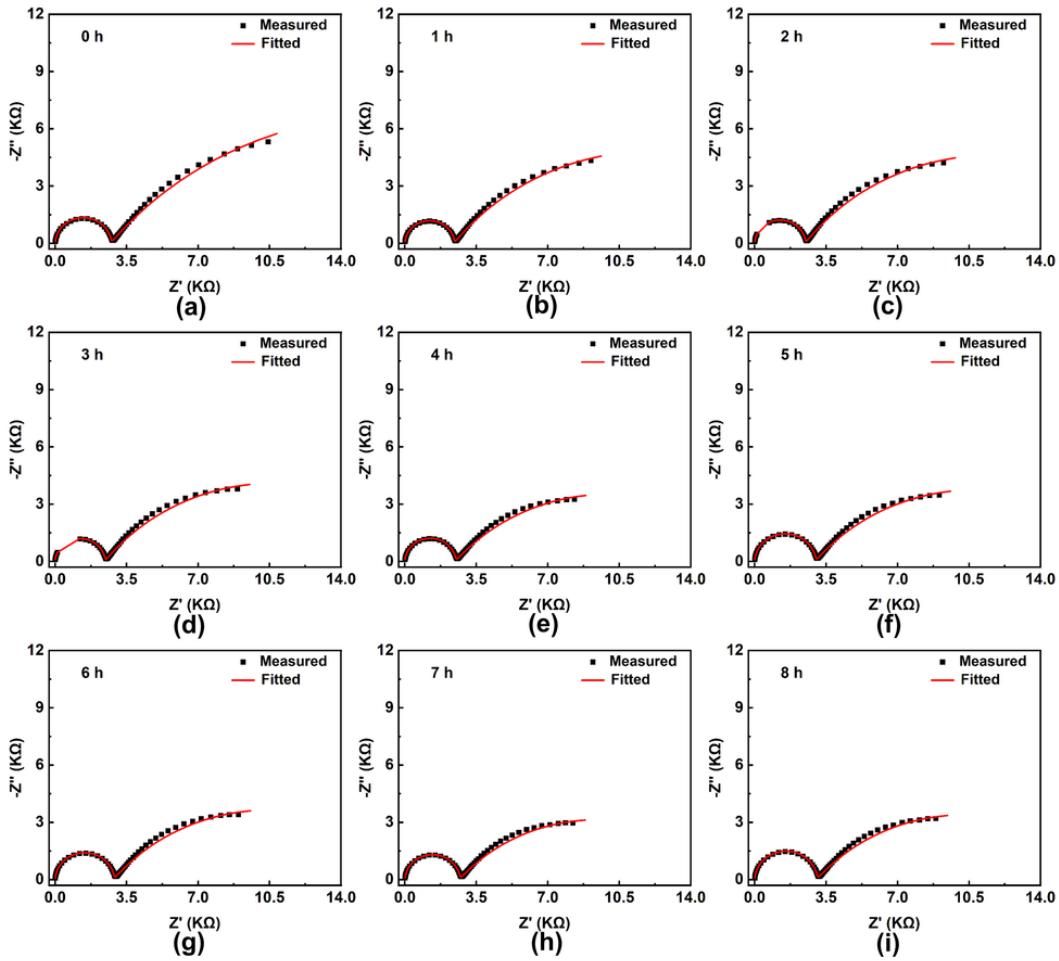

Fig. S15 Time-dependent Nyquist plots of **Pr-Hpda-H_2O** recorded at 298 K and ~97% RH after different exposure times: 0 h (a), 1 h (b), 2 h (c), 3 h (d), 4 h (e), 5 h (f), 6 h (g), 7 h (h), and 8 h (i).

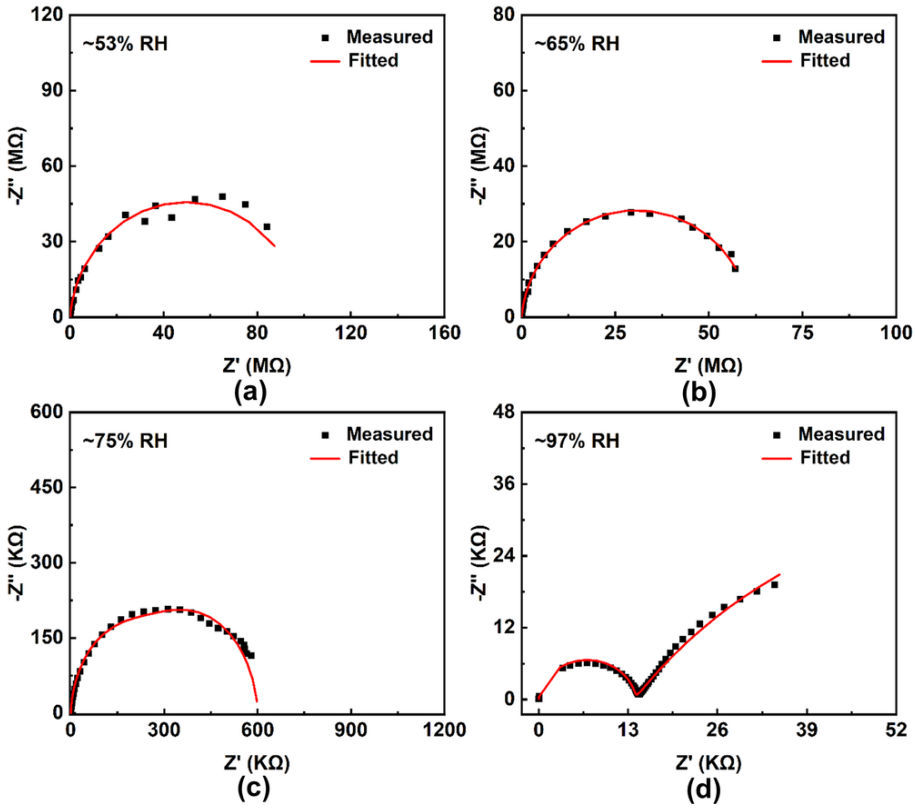

Fig. S16 Nyquist plots of **Pr-pda-H_2O** recorded at 298 K under different relative humidities: 53% RH (a), 65% RH (b), 75% RH (c), and 97% RH (d).

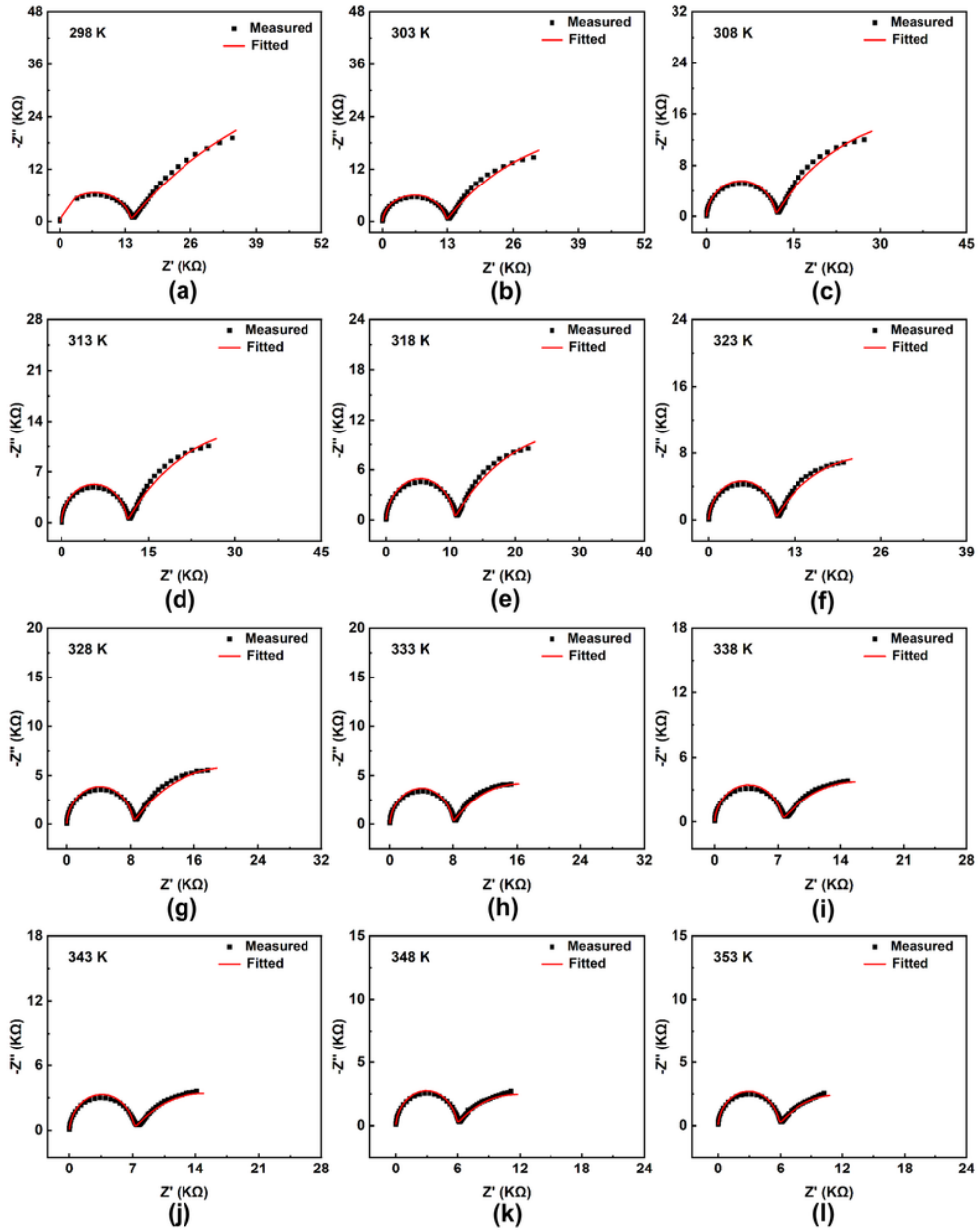

Fig. S17 Nyquist plots of **Pr-pda-H_2O** measured at ~97% RH and temperatures of (a) 298 K, (b) 303 K, (c) 308 K, (d) 313 K, (e) 318 K, (f) 323 K, (g) 328 K, (h) 333 K, (i) 338 K, (j) 343 K, (k) 348 K, and (l) 353 K.

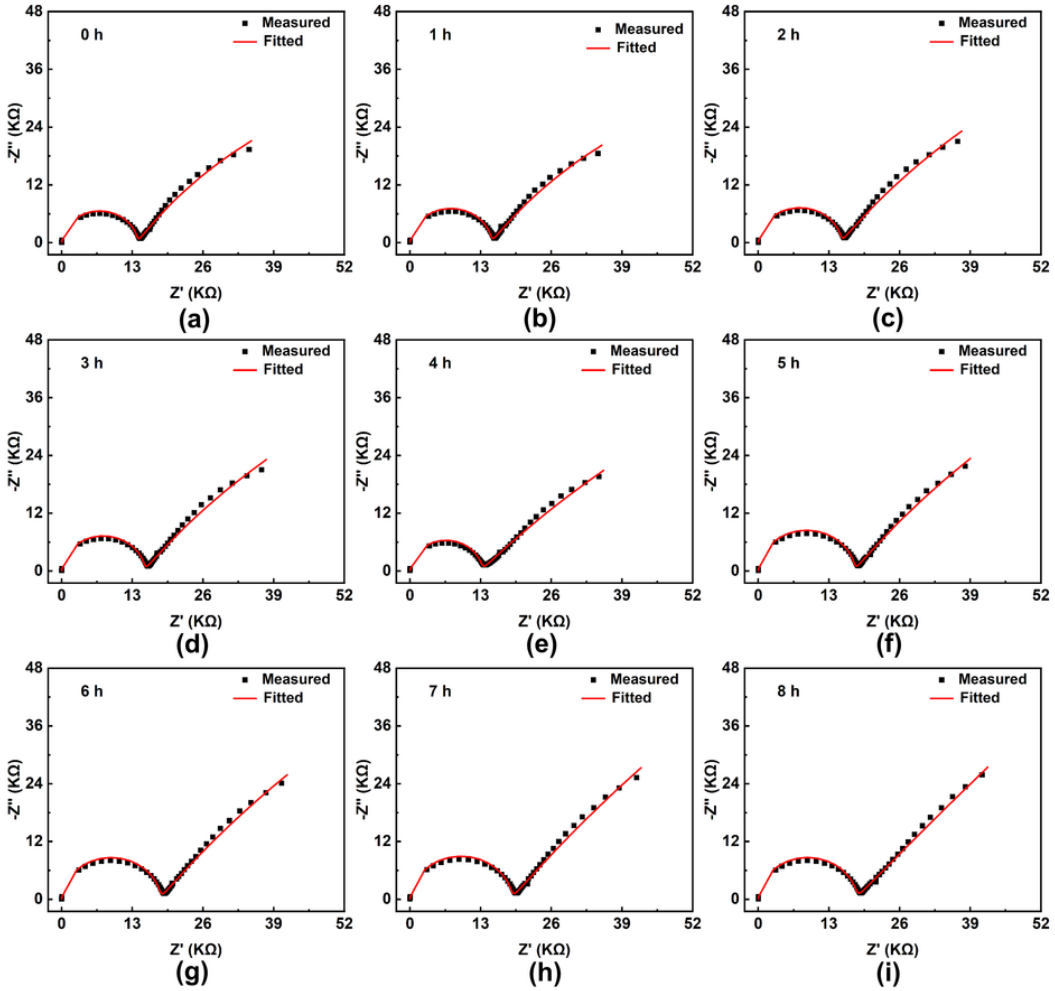

Fig. S18 Time-dependent Nyquist plots of **Pr-pda-H_2O** recorded at 298 K and ~97% RH after different exposure times: 0 h (a), 1 h (b), 2 h (c), 3 h (d), 4 h (e), 5 h (f), 6 h (g), 7 h (h), and 8 h (i).

• **Proton conductivity data**

Table S11 Proton conductivities of **Pr-Ce-H_2pda-H_2O**, **Pr-Hpda-H_2O** and **Pr-pda-H_2O** at 298 K under different RH conditions

Conditions	Conductivity		
	Pr-Ce-H_2pda-H_2O	Pr-Hpda-H_2O	Pr-pda-H_2O
~97% RH	1.16×10^{-3} S cm^{-1}	7.63×10^{-4} S cm^{-1}	1.28×10^{-4} S cm^{-1}
~75% RH	1.67×10^{-4} S cm^{-1}	7.04×10^{-5} S cm^{-1}	3.28×10^{-6} S cm^{-1}
~65% RH	9.37×10^{-8} S cm^{-1}	3.43×10^{-8} S cm^{-1}	2.57×10^{-8} S cm^{-1}
~53% RH	5.46×10^{-8} S cm^{-1}	2.5×10^{-8} S cm^{-1}	1.42×10^{-8} S cm^{-1}

Table S12 Proton conductivities of **Pr-Ce-H_2pda-H_2O**, **Pr-Hpda-H_2O** and **Pr-pda-H_2O** at ~97% RH under different temperatures

Conditions	Conductivity		
	Pr-Ce-H_2pda-H_2O	Pr-Hpda-H_2O	Pr-pda-H_2O
288 K	-	6.8×10^{-4} S cm^{-1}	-
290 K	-	6.93×10^{-4} S cm^{-1}	-
292 K	-	7.04×10^{-4} S cm^{-1}	-
294 K	-	7.25×10^{-4} S cm^{-1}	-
296 K	-	7.49×10^{-4} S cm^{-1}	-
298K	1.16×10^{-3} S cm^{-1}	7.63×10^{-4} S cm^{-1}	1.28×10^{-4} S cm^{-1}
303 K	1.21×10^{-3} S cm^{-1}	8.18×10^{-4} S cm^{-1}	1.41×10^{-4} S cm^{-1}
308 K	1.54×10^{-3} S cm^{-1}	8.81×10^{-4} S cm^{-1}	1.51×10^{-4} S cm^{-1}
313 K	1.74×10^{-3} S cm^{-1}	1.07×10^{-3} S cm^{-1}	1.58×10^{-4} S cm^{-1}
318 K	2.10×10^{-3} S cm^{-1}	1.19×10^{-3} S cm^{-1}	1.68×10^{-4} S cm^{-1}
323 K	2.26×10^{-3} S cm^{-1}	1.33×10^{-3} S cm^{-1}	1.78×10^{-4} S cm^{-1}
328 K	2.92×10^{-3} S cm^{-1}	1.62×10^{-3} S cm^{-1}	2.15×10^{-4} S cm^{-1}
333 K	3.34×10^{-3} S cm^{-1}	1.84×10^{-3} S cm^{-1}	2.24×10^{-4} S cm^{-1}
338 K	3.86×10^{-3} S cm^{-1}	2.2×10^{-3} S cm^{-1}	2.38×10^{-4} S cm^{-1}
343 K	4.63×10^{-3} S cm^{-1}	2.39×10^{-3} S cm^{-1}	2.46×10^{-4} S cm^{-1}
348 K	4.75×10^{-3} S cm^{-1}	2.67×10^{-3} S cm^{-1}	3.01×10^{-4} S cm^{-1}
353 K	5.54×10^{-3} S cm^{-1}	3.12×10^{-3} S cm^{-1}	3.07×10^{-4} S cm^{-1}

Table S13 Proton conductivities of **Pr-Ce-H_2pda-H_2O**, **Pr-Hpda-H_2O** and **Pr-pda-H_2O** at ~97% RH under different temperatures

Conditions	Conductivity		
	Pr-Ce-H_2pda-H_2O	Pr-Hpda-H_2O	Pr-pda-H_2O
0 h	1.16×10^{-3} S cm^{-1}	7.65×10^{-4} S cm^{-1}	1.28×10^{-4} S cm^{-1}
1 h	8.90×10^{-4} S cm^{-1}	8.68×10^{-4} S cm^{-1}	1.28×10^{-4} S cm^{-1}
2 h	9.17×10^{-4} S cm^{-1}	8.51×10^{-4} S cm^{-1}	1.19×10^{-4} S cm^{-1}
3 h	8.75×10^{-4} S cm^{-1}	8.64×10^{-4} S cm^{-1}	1.17×10^{-4} S cm^{-1}
4 h	8.95×10^{-4} S cm^{-1}	8.42×10^{-4} S cm^{-1}	1.69×10^{-4} S cm^{-1}
5 h	8.24×10^{-4} S cm^{-1}	7.07×10^{-4} S cm^{-1}	1.34×10^{-4} S cm^{-1}
6 h	8.79×10^{-4} S cm^{-1}	7.27×10^{-4} S cm^{-1}	1.01×10^{-4} S cm^{-1}
7 h	5.91×10^{-4} S cm^{-1}	7.81×10^{-4} S cm^{-1}	9.83×10^{-5} S cm^{-1}
8 h	7.70×10^{-4} S cm^{-1}	6.79×10^{-4} S cm^{-1}	9.52×10^{-5} S cm^{-1}

XII. PXRD patterns after impedance measurements.

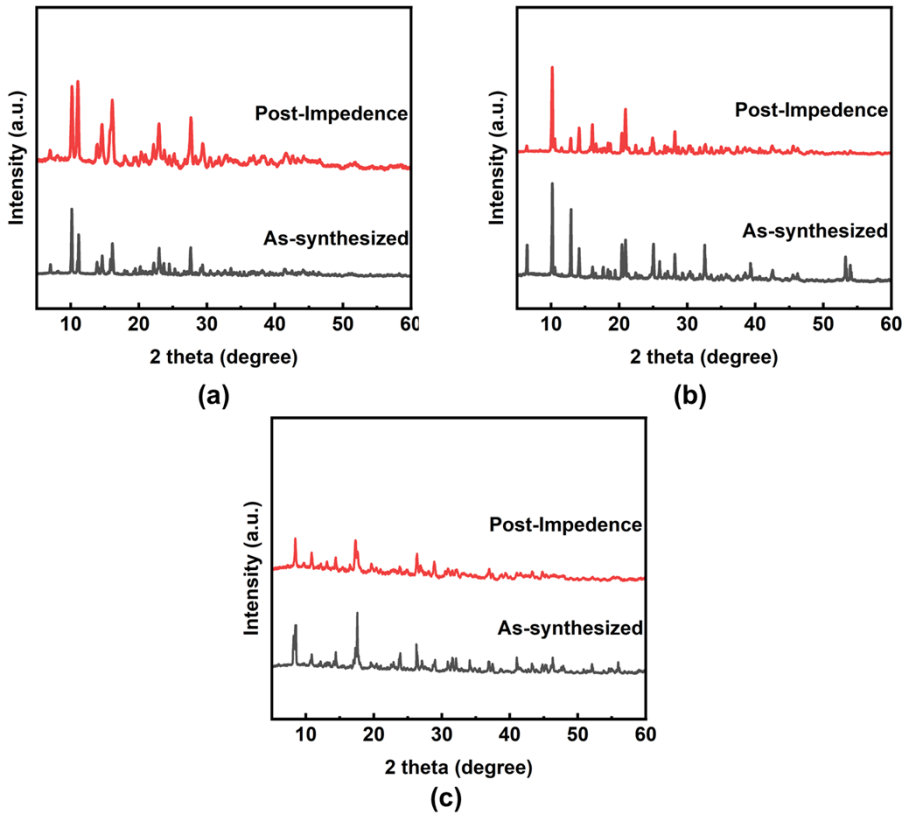

Fig. S19 PXRD patterns of **Pr-Ce-H_2pda-H_2O** (a), **Pr-Hpda-H_2O** (b) and **Pr-pda-H_2O** (c) comparing the as-synthesized samples with those collected after impedance measurements under ~97% RH.

XIII. Comparison of proton conductivity

Table S14 Comparison of proton conductivity of **Pr-Ce-H_2pda-H_2O**, **Pr-Hpda-H_2O** and **Pr-pda-H_2O** with representative reported proton conductors

Materials	σ (S cm^{-1})	E_a (eV)	T (K)	RH (%)	Reference
Pr-Ce-H_2pda-H_2O	5.54×10^{-3}	0.311	353	~97	This work
Pr-Hpda-H_2O	3.12×10^{-3}	0.126/0.288	353	~97	This work
Pr-pda-H_2O	3.07×10^{-4}	0.152	353	~97	This work
$[Zn(PDA)_{0.5}(HPDA)(H_2MDP)]_n$ [a]	4.63×10^{-4}	0.279	353	90	[22]
$\{[(H_3O^+)_2][Zn(pzdc)_2]\}_n$ [b]	2.42×10^{-3}	0.21	323	~97	[23]
$\{[(H_3O^+)_2][Mn(pzdc)_2]\}_n$	2.03×10^{-3}	0.10	323	~97	[23]
$[Cu(Hpzdc)_2\cdot2H_2O]_n$	1.68×10^{-3}	0.35	323	~97	[23]
Urea-MOF-74 (Ni)	2.34×10^{-3}	0.37	328	95	[24]
$PMoV_2$@MIL-101	6.31×10^{-3}	0.11	353	98	[25]
$(Me_2NH_2)[Ba(L^2)(H_2O)]\cdot3H_2O$ [c]	4.47×10^{-3}	0.51	358	98	[26]
$\{NBu_2(CH_2COOH)_2\}[MnCr(ox)_3]$	1.8×10^{-3}	0.31	298	98	[27]
$[Zn(L)Cl]_n$ [d]	4.72×10^{-3}	0.37	373	98	[28]
BUT-76	8.55×10^{-3}	0.26	353	100	[29]
$Zn_2(\mu\text{-}OH)(dia)_2(sip)\cdot2H_2O$[e]	1.8×10^{-3}	0.28	358	98	[30]
$Co(dia)_{1.5}(Hsip)(H_2O)\cdot H_2O$	4.2×10^{-4}	0.39	358	98	[30]
UPC-H5	5.59×10^{-4}	0.23	303	95	[31]
UPC-H5a	7.00×10^{-3}	0.20	303	95	[31]
PHOS-100(Hf)	4.77×10^{-4}	0.83	298	95	[32]
$[Eu_2(TTHA)(H_2O)_4]\cdot9H_2O$ [f]	3.5×10^{-3}	0.44	353	98	[33]
MFM-722(Pb)-H_2O	6.61×10^{-4}	0.21	323	98	[34]
$[Cu_2(o\text{-}CPH_2IDC)_2(phen)_2]\cdot3H_2O$ [g]	3.13×10^{-4}	0.45	373	100	[35]
$[Zn(p\text{-}IPhH_2DC)]_n$ [h]	1.9×10^{-3}	1.48	373	98	[36]
$[Co(p\text{-}IPhH_2DC)]_n$	1.07×10^{-3}	1.28	373	98	[36]
$Tm_2Ni_3(oda)_6(H_2O)_6\cdot14H_2O$ [i]	2.43×10^{-3}	1.46	343	100	[37]
$Na_3H_{10}[Ni(H_2O)_2(VO)_6(B_{10}O_{22})_2]\cdot NH_4$	3.22×10^{-3}	1.26	323	100	[38]

·19H_2O					
IPCE-2Pd	8.11×10^{-3}	0.518	368	95	[39]
Cu-SAT	2.27×10^{-3}	0.65	353	95	[40]
Ca-NDS [j]	1.46×10^{-3}	0.68	353	95	[40]
Cu-SQAT	1.11×10^{-3}	0.81	353	95	[40]
TGU-11	3.14×10^{-4}	0.18	363	100	[41]
$\{Cd_2(D\text{-}pmpcH)H_2O)_2Cl_2\}_n$	1.38×10^{-4}	0.14	323	~97	[42]
$\{[Er_3(pmpc)(C_2O_4)_3(H_2O)_7]$ ·$2H_2O\}_n$	9.3×10^{-5}	0.33	303	~97	[43]
$[(H_3betc)(H\text{-}Hopip)_{0.5}(H_2O)]$	1.38×10^{-4}	0.41	299	~97	[44]
$[(H_3betc)_2(H_2\text{-}Mepip)(H_2O)]$	3.72×10^{-4}	0.21	299	~97	[44]
$[Co(PPA)_2(BDC)(H_2O)_2\cdot(PPA)_2$ $(H_2BDC)_2(H_2O)]$	2.29×10^{-4}	0.24	325	~97	[45]

Note: σ = Proton conductivity; E_a = Activation energy; T = Temperature; RH = Relative humidity. [a] H_2PDA = 1,4-phenyl diacetic acid. H_2MDP = m-benzenedipropionic acid; [b] H_2pzdc = 2,3-pyrazinedicarboxylic acid. [c] L = 1H-tetrazole-5-acetic acid; [d] L = 1H-benzimidazole-5-carboxylic acid; [e] dia = 9,10-di(1H-imidazol-1-yl)anthracene; H_2sip = 5-sulfoisophthalic acid;[f] TTHA = 1,3,5-triazine-2,4,6-triamine hexaacetic acid; [g] H_3o-CPH-IDC = 2-(2-carboxylphenyl)-1H-imidazole-4,5-dicarboxylic acid; phen = 1,10-phenanthroline; [h] H_4p-IPhH_2DC = 5-phosphonoisophthalic acid; [i] oda = oxydiacetate; [j] NDS = 1,5-naphthalenedisulfonate.

XIV. Hydrophilicity: water contact angles

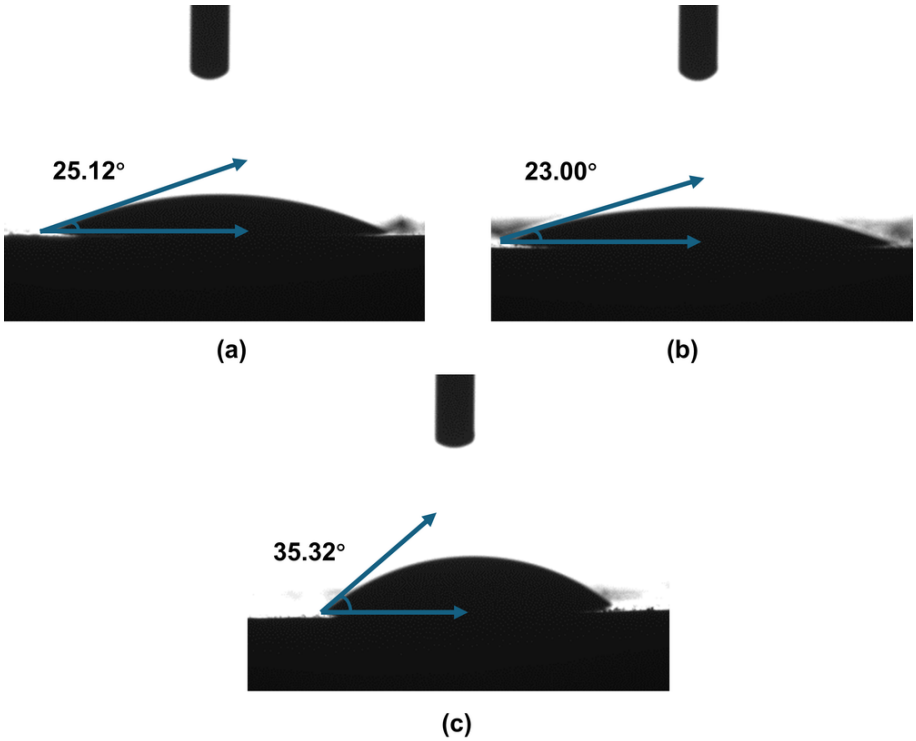

Fig. S20 Water contact angle measurements of **Pr-Ce-H_2pda-H_2O** (a), **Pr-Hpda-H_2O** (b), and **Pr-pda-H_2O** (c).

XV. Hydrophilicity: water vapor adsorption–desorption isotherms

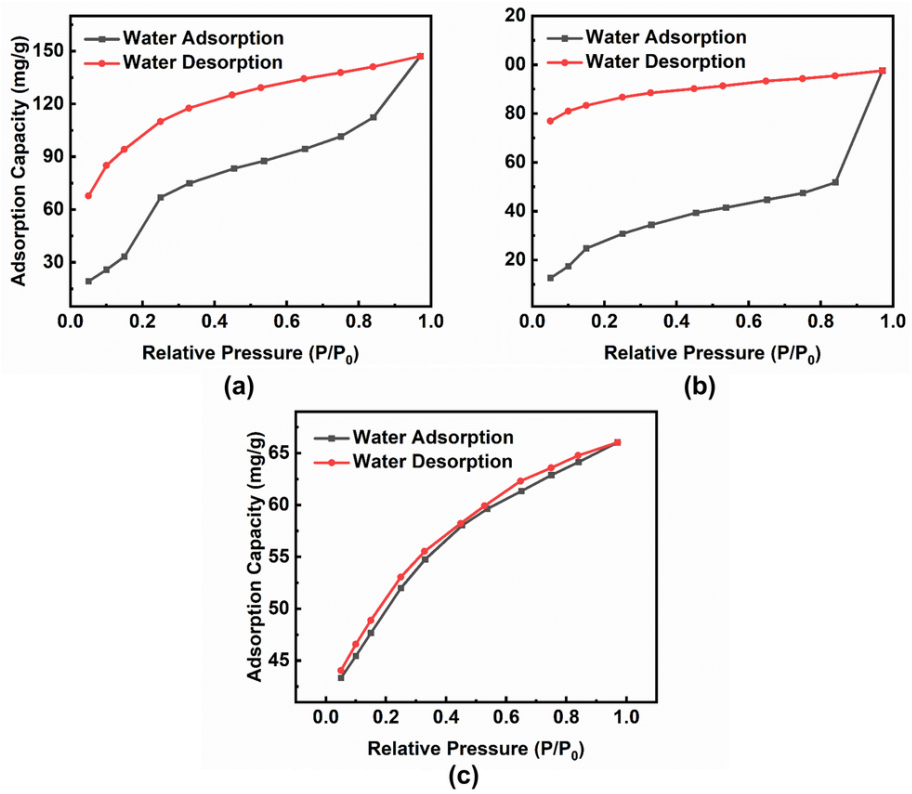

Fig. S21 Water vapor adsorption–desorption isotherms of **Pr-Ce-H_2pda-H_2O** (a), **Pr-Hpda-H_2O** (b), and **Pr-pda-H_2O** (c) measured at 298 K.

Experimental details of water vapor adsorption–desorption measurements: For the water vapor adsorption-desorption experiments, the measurements were carried out at 298 K using a BSD-VVS gravimetric vapor sorption analyzer. Before measurement, the samples were degassed under vacuum at 333 K for 3 h. During adsorption, the relative pressure (P/P_0) was increased from 0.05 to 0.95, and during desorption it was decreased from 0.95 back to 0.05. Ten representative pressure points were selected for each branch. These points were not chosen as densely as in volumetric measurements, but were instead selected according to the characteristics of the gravimetric method in order to reflect the overall adsorption-desorption trend under representative humidity conditions. Some of these points also correspond to commonly encountered humidity ranges, which facilitates comparison with the proton conductivity measurements performed under salt-controlled relative humidity. At each pressure step, equilibrium was considered to be reached when the change in adsorbed mass was less than 0.1 mg over 30 min under H_2O vapor. For samples that were difficult to equilibrate, a maximum equilibration time of 180 min was applied.

XVI. Proton dissociation from ligand

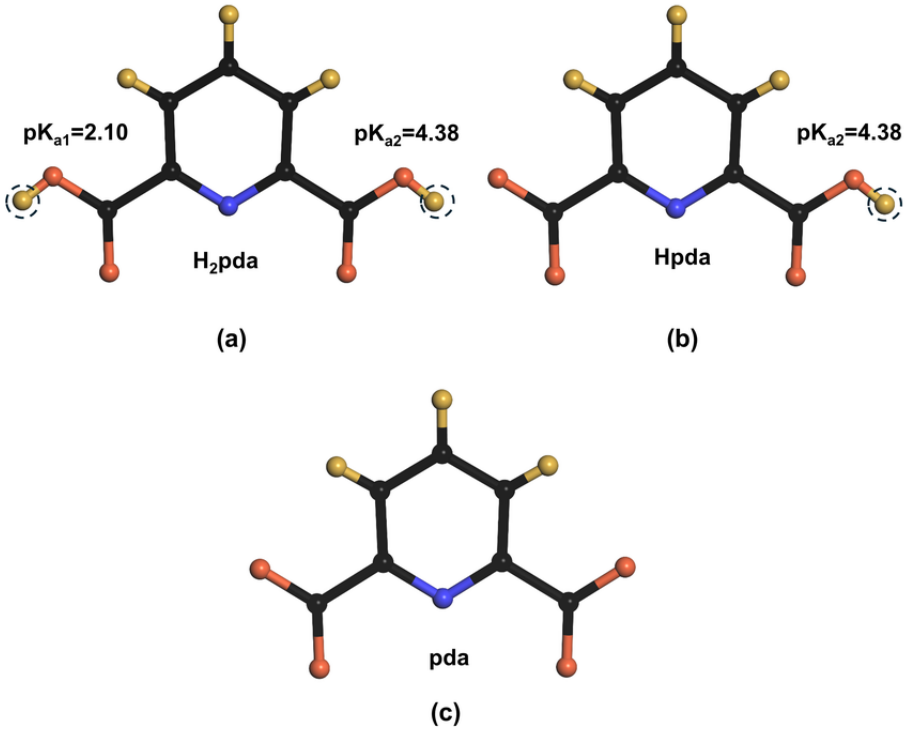

Fig. S22 Schematic structures of **H_2pda** (a), **Hpda** (b), and **pda** (c), showing the dissociable carboxylic protons and the corresponding pK_a values.

XVII. Dielectric measurements

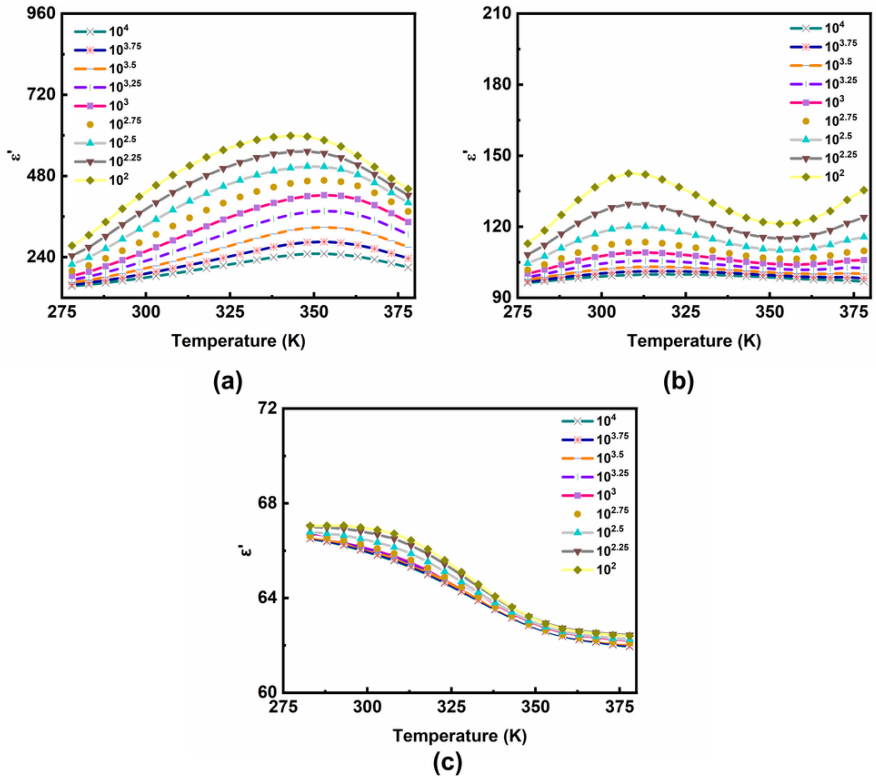

Fig. S23 Frequency dependence of the dielectric constant (ε′) for **Pr-Ce-H$_2$pda-H$_2$O** (a), **Pr-Hpda-H$_2$O** (b) and **Pr-pda-H$_2$O** (c).

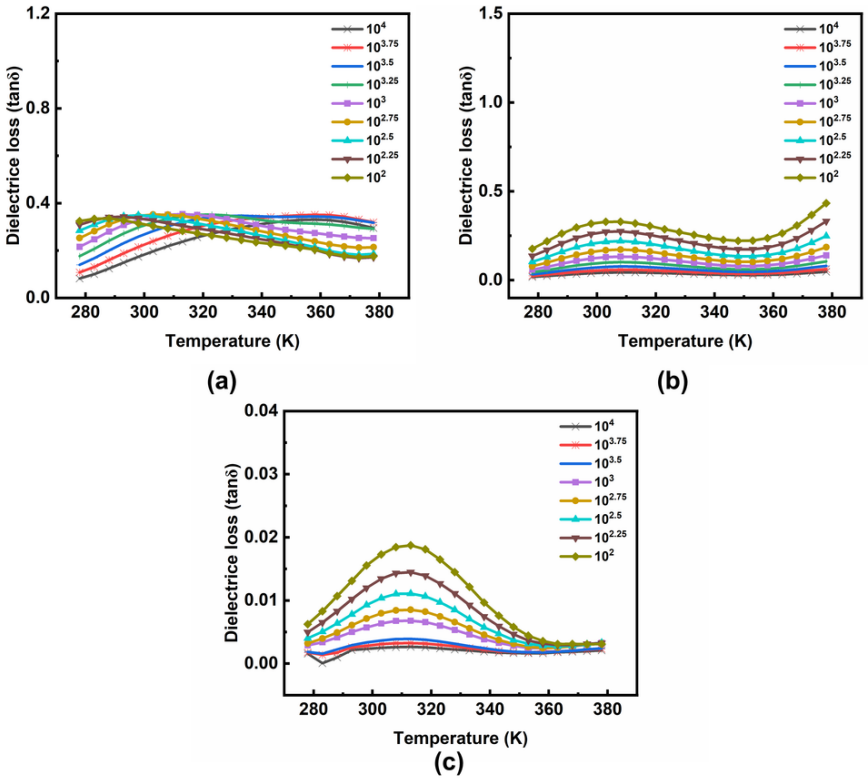

Fig. S24 Frequency dependence of the dielectric loss (tanδ) for **Pr-Ce-H$_2$pda-H$_2$O** (a), **Pr-Hpda-H$_2$O** (b) and **Pr-pda-H$_2$O** (c).

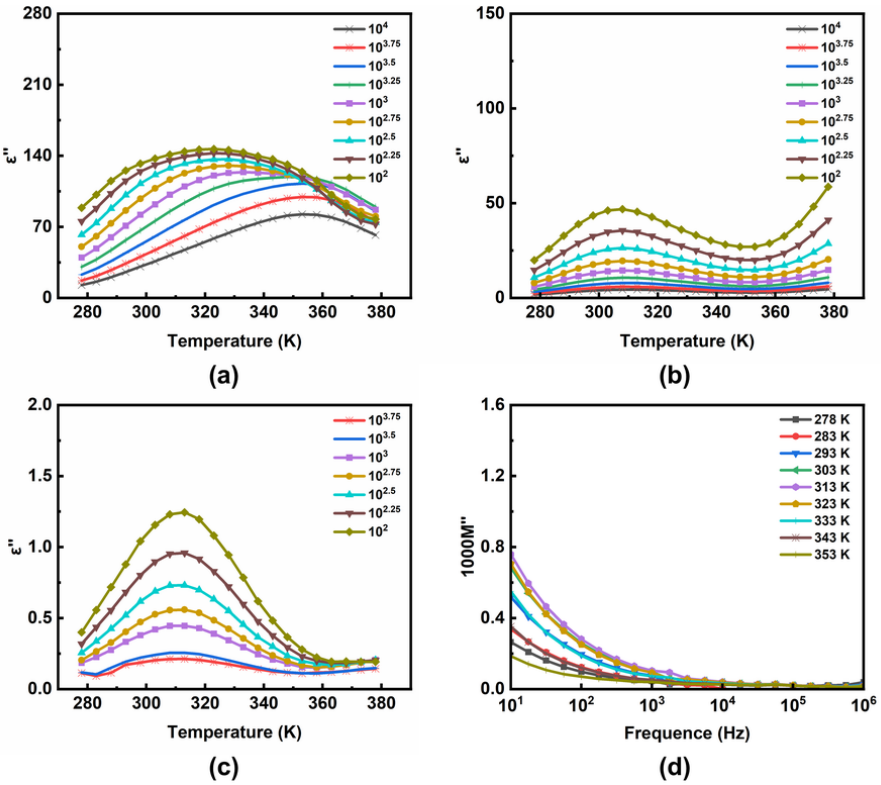

Fig. S25 Frequency dependence of the dielectric loss factor (ε′′) for **Pr-Ce-H$_2$pda-H$_2$O** (a), **Pr-Hpda-H$_2$O** (b) and **Pr-pda-H$_2$O** (c). (d) Frequency–dependent M″ spectrum for **Pr-pda-H$_2$O** (278–353 K).

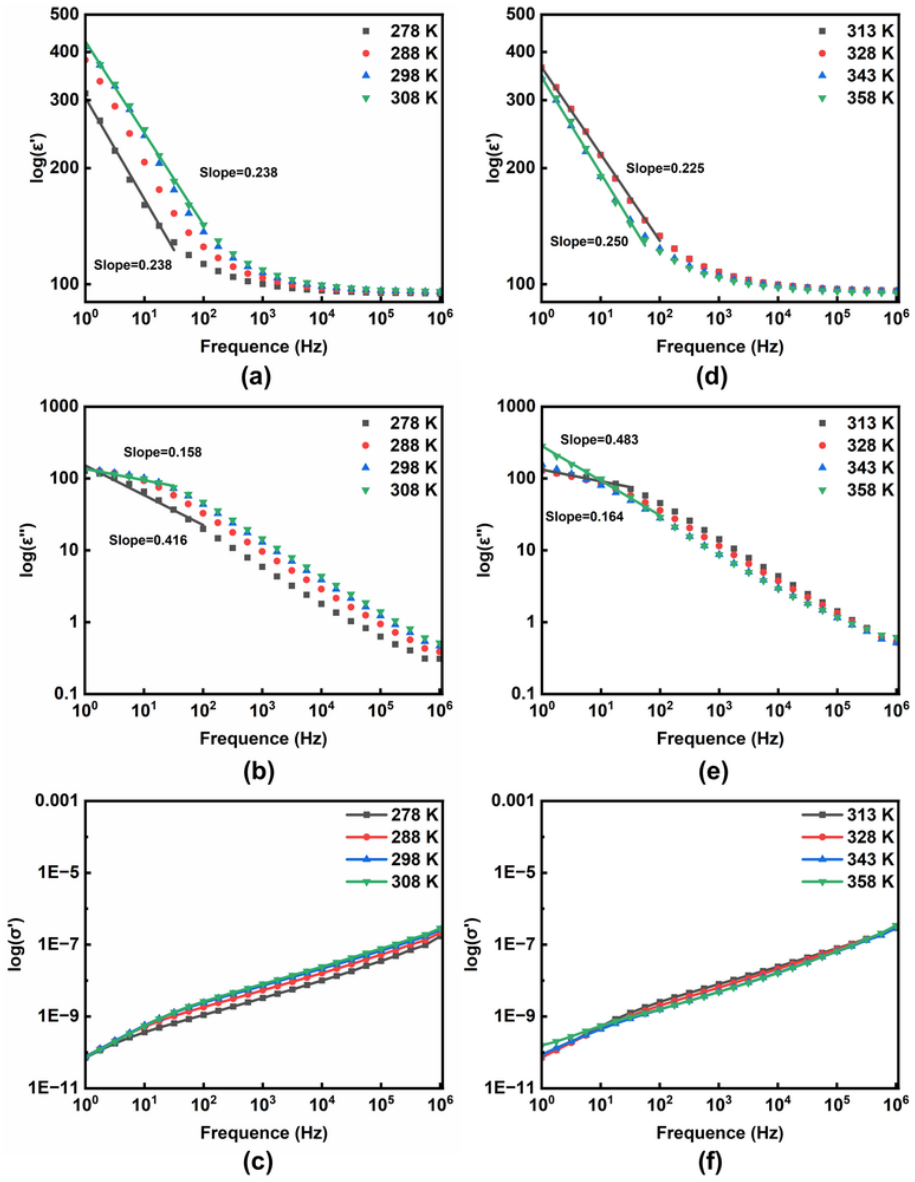

Fig. S26 Frequency dependence of dielectric and conductivity spectra for **Pr-Hpda-H_2O**: (a–c) low-temperature range and (d–f) high-temperature range. Plots show (a, d) logε′−log*f*, (b, e) logε''−log*f* and logσ'−log*f* (c, f).

XVIII. Fitting of Cole-Cole plots

Table S15 M_0, M_∞ and α parameters obtained from the best fits for **Pr-Ce-H_2pda-H_2O**

T / K	M_0	M_∞	α	R^2
278 K	0.007038	0.001428	0.514885	0.9976
283 K	0.007	0.001387	0.515549	0.9965
293 K	0.006907	0.001288	0.515672	0.9955
298 K	0.006879	0.001247	0.513113	0.9945
313 K	0.006804	0.001191	0.506143	0.9952
323 K	0.006772	0.001177	0.498717	0.9927
343 K	0.00671	0.001239	0.493344	0.9910
353 K	0.006635	0.001353	0.515821	0.9767

Table S16 M_0, M_∞ and α parameters obtained from the best fits for **Pr-Hpda-H_2O**

T / K	M_0	M_∞	α	R^2
278 K	0.010525	0.001479	0.56882	0.9994
288 K	0.010491	0.001557	0.568242	0.9991
298 K	0.010478	0.001592	0.565965	0.9985
308 K	0.01045	0.001691	0.551124	0.9971
313 K	0.010441	0.001711	0.543832	0.9964
328 K	0.010430	0.001706	0.519560	0.9958
343 K	0.010420	0.001671	0.519609	0.9950
358 K	0.010408	0.001599	0.523892	0.9918

XIX. Proton-conduction activation energy: Arrhenius fitting

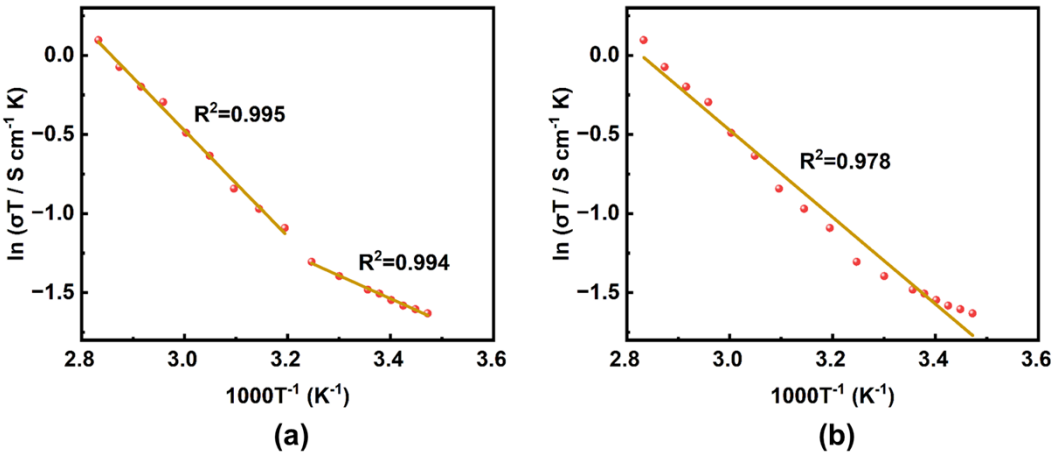

Fig. S27 Proton conduction activation energy analysis for **Pr-Hpda-H_2O**. (a) Arrhenius plot showing a dual-segment linear fit, indicating a change in the conduction mechanism. (b) Arrhenius plot showing a single-segment linear fit.

XX. Comparison of dielectric constant

Table S17 Comparison of the dielectric constant (ε′) of **Pr-Ce-H_2pda-H_2O**, **Pr-Hpda-H_2O** and **Pr-pda-H_2O** with representative reported materials

Materials	Dielectric constant	Frequency (Hz)	Reference
Pr-Ce-H_2pda-H_2O	599	10^2	This work
Pr-Hpda-H_2O	143	10^2	This work
Pr-pda-H_2O	67	10^2	This work
Co-2PPA [a]	620	10^2	[46]
Co-4PPA	630	10^2	[46]
(CBQ)CuI 3$(CN)_3$Br [b]	119.3	-	[47]
[Sm_2(bhc)$(H_2O)_6$]n [c]	45.1	5×10^3	[48]
Na[In_3(odpt)$_2$$(OH)_2$$(H_2O)_2$]$(H_2O)_4$ [d]	40.5	10^3	[49]
Cu:PI-Bpy (1:2) [e]	133	10^2	[50]
$BaTiO_3$/PEGDA [f]	40	10^3	[51]
$BaTiO_3$/TMPTA [g]	28	10^3	[51]
$BaTiO_3$/TDDMA[h]	19	10^3	[51]
Ni_2(1,4-bdc)$_2$(dabco)·[3DMF·1/2H_2O] [i]	100	10^2	[52]
Co_2(1,4-bdc-NH_2)$_2$(dabco)·[7/2DMF·1H_2O]	6	10^3	[52]
Ni_2(1,4-bdc)$_2$(dabco)	10	10^2	[52]
$[NH_2(CH_3)_2]_n[Fe^{3+}Fe^{2+}_{(1-x)}Ni^{2+}_x(HCOO)_6]_n$	1350	10^2	[53]
$[NH_2(CH_3)_2]_n[Fe^{3+}Fe^{2+}(HCOO)_6]_n$	800	10^2	[53]
$[NH_2(CH_3)_2]_n[Fe^{3+}Fe^{2+}(HCOO)_6]_n$	50	10^2	[53]
$[NH_2(CH_3)_2]_n[Fe^{3+}Co^{2+}_{(1-x)}Ni^{2+}_x(HCOO)_6]_n$	400	10^2	[54]
[Mg(phen)(bdc)]$_n$ [j]	3.3	10^2	[54]
$[(CH_3)_2NH_2][Mg(HCOO)_3]$	16	10^2	[54]
[Cu(CA)]·$CH_3CN\}_n$	44	10^2	[55]
{[Cu(CA)$(H_2O)_2$]·$H_2O\}_n$	35	10^2	[55]
$[Ag_2(CA)]_n$	321	10^2	[55]

[a] PPA = 4-(3-pyridinyl)-2-amino pyrimidine. [b] CBQ-Br = N-4-cyanobenzyl quinidinium. [c] H_6bhc = benzenehexacarboxylic acid. [d] odpt = 4,4′-oxydiphthalate. [e] Bpy = (5,5′-bis[(4-amino)phenoxy]-2,2′-bipyrimidine). [f] PEGDA = Poly (ethylene glycol) diacrylate. [g] TMPTA = Trimethylolpropane triacrylate. [h]TDDMA = 1,14-tetrade-canediol dimethacrylate . [i] dabco = 1,4-diazabicyclo-[2.2.2]octane. [j] phen = 1,10-phenanthroline, bdc^{2-} = 1,4-benzenedicarboxylate.

XXI. References for Supporting Information

1 T. K. Prasad and M. V. Rajasekharan, Cerium(IV)-lanthanide(III)-pyridine-2,6-dicarboxylic acid system: coordination salts, chains, and rings, *Inorg. Chem.*, 2009, **48**, 11543–11550.

2 B. Zhao, L. Yi, Y. Dai, X. Y. Chen, P. Cheng, D. Z. Liao, S. P. Yan and Z. H. Jiang, Systematic investigation of the hydrothermal syntheses of Pr(III)-PDA (PDA = pyridine-2,6-dicarboxylate anion) metal-organic frameworks, *Inorg. Chem.*, 2005, **44**, 911–920.

3 C. Zhang, S. Wei, L. Sun, F. Xu, P. Huang and H. Peng, Synthesis, structure and photocatalysis properties of two 3D isostructural Ln(III)-MOFs based on 2,6-pyridinedicarboxylic acid, *J. Mater. Sci. Technol.*, 2018, **34**, 1526–1531.

4 S. Van Gele, S. Bette and B. V. Lotsch, The devil is in the details: pitfalls and ambiguities in the analysis of x-ray powder diffraction data of 2D covalent organic frameworks, *JACS Au*, 2025, **5**, 388–398.

5 P. Bindu and S. Thomas, Estimation of lattice strain in ZnO nanoparticles: x-ray peak profile analysis, *J. Theor. Appl. Phys.*, 2014, **8**, 123–134.

6 T. R. Gupta, S. S. Sidhu, J. K. Katiyar and H. S. Payal, Measurements of lattice strain in cold-rolled CR4 steel sheets using x-ray diffraction, *Mater. Sci. Eng., B*, 2021, **264**, 114930.

7 B. H. Hwang and S. F. Tu, A method for obtaining the error of a peak position due to counting statistics, *Powder Diffr.*, 1995, **10**, 148–151.

8 J. Tang, F. Zhang, X. Liang, G. Dai and F. Qu, Abundant defects of zirconium-organic xerogels: high anhydrous proton conductivities over a wide temperature range and formic acid impedance sensing, *J. Colloid Interface Sci.*, 2022, **607**, 181–191.

9 Z. Li, M. M. Dawley, I. Carmichael and S. Ptasińska, Electron-induced fragmentation of methylated formamides, *Int. J. Mass Spectrom.*, 2016, **410**, 36–46.

10 D. Feng, K. Wang, J. Su, T. F. Liu, J. Park, Z. Wei, M. Bosch, A. Yakovenko, X. Zou and H. C. Zhou, A highly stable zeotype mesoporous zirconium metal-organic framework with ultralarge pores, *Angew. Chem., Int. Ed.*, 2015, **54**, 149–154.

11 Y. Q. Jiao, H. Y. Zang, X. L. Wang, E. L. Zhou, B. Q. Song, C. G. Wang, K. Z. Shao and Z. M. Su, Self-assembled arrays of polyoxometalate-based metal-organic nanotubes for proton conduction and magnetism, *Chem. Commun.*, 2015, **51**, 11313–11316.

12 S. Rodriguez-Hermida, M. Y. Tsang, C. Vignatti, K. C. Stylianou, V. Guillerm, J. Perez-Carvajal, F. Teixidor, C. Vinas, D. Choquesillo-Lazarte, C. Verdugo-Escamilla, I. Peral, J. Juanhuix, A. Verdaguer, I. Imaz, D. Maspoch and J. Giner Planas, Switchable surface hydrophobicity-hydrophilicity of a metal-organic framework, *Angew. Chem., Int. Ed.*, 2016, **55**, 16049–16053.

13 F. Leng, H. Liu, M. Ding, Q.-P. Lin and H.-L. Jiang, Boosting photocatalytic hydrogen production of porphyrinic MOFs: the metal location in metalloporphyrin matters, *ACS Catal.*, 2018, **8**, 4583–4590.

14 H. L. Jiang, D. Feng, K. Wang, Z. Y. Gu, Z. Wei, Y. P. Chen and H. C. Zhou, An exceptionally stable, porphyrinic Zr metal-organic framework exhibiting pH-dependent fluorescence, *J. Am. Chem. Soc.*, 2013, **135**, 13934–13938.

15 D. Feng, T. F. Liu, J. Su, M. Bosch, Z. Wei, W. Wan, D. Yuan, Y. P. Chen, X. Wang, K. Wang, X. Lian, Z. Y. Gu, J. Park, X. Zou and H. C. Zhou, Stable metal-organic frameworks containing single-molecule traps for enzyme encapsulation, *Nat. Commun.*, 2015, **6**, 5979.

16 J. Kang, N. A. Khan, E. Haque and S. H. Jhung, Chemical and thermal stability of isotypic metal-organic frameworks: effect of metal ions, *Chem. – Eur. J.*, 2011, **17**, 6437–6442.

17 A. Pankajakshan, M. Sinha, A. A. Ojha and S. Mandal, Water-stable nanoscale zirconium-based metal-organic frameworks for the effective removal of glyphosate from aqueous media, *ACS Omega*, 2018, **3**, 7832–7839.

18 Y. Zhang, Q. Ruan, Y. Peng, G. Han, H. Huang and C. Zhong, Synthesis of hierarchical-pore metal-organic framework on liter scale for large organic pollutants capture in wastewater, *J. Colloid Interface Sci.*, 2018, **525**, 39–47.

19 S. Dhaka, R. Kumar, A. Deep, M. B. Kurade, S.-W. Ji and B.-H. Jeon, Metal–organic frameworks (MOFs) for the removal of emerging contaminants from aquatic environments, *Coord. Chem. Rev.*, 2019, **380**, 330–352.

20 Z. Hasan, E.-J. Choi and S. H. Jhung, Adsorption of naproxen and clofibric acid over a metal–organic framework MIL-101 functionalized with acidic and basic groups, *Chem. Eng. J.*, 2013, **219**, 537–544.

21 S. Wang, F. Xie, S. Zhang, X. Liang, Q. Gao, Y. Chen, F. Zhang, C. Wen, L. Feng and C. Wan, Water-assisted proton conduction regulated by hydrophilic groups in metallo-hydrogen-bonded organic frameworks: “like-attracts-like” between hydrophilic groups and water molecules, *CrystEngComm*, 2023, **25**, 4701–4715.

22 F. Ambroz, T. J. Macdonald, V. Martis and I. P. Parkin, Evaluation of the BET

theory for the characterization of meso and microporous MOFs, *Small Methods*, 2018, **2**, 1800173.

23 X. Liang, S. Wang, S. Zhang, C. Lin, F. Xie, R. Li, F. Zhang, C. Wen, L. Feng and C. Wan, High proton conductivity modulated by active protons in 1D ultra-stable metal–organic coordination polymers: a new insight into the coordination interaction/ability of metal ions, *Inorg. Chem. Front.*, 2023, **10**, 1238–1254.

24 M. K. Sarango-Ramirez, D. W. Lim, D. I. Kolokolov, A. E. Khudozhitkov, A. G. Stepanov and H. Kitagawa, Superprotonic conductivity in metal-organic framework via solvent-free coordinative urea insertion, *J. Am. Chem. Soc.*, 2020, **142**, 6861–6865.

25 F. Wang, C. Liang, J. Tang, F. Zhang and F. Qu, The promotion of proton conductivity by immobilizing molybdovanadophosphoric acids in metal–organic frameworks, *New J. Chem.*, 2020, **44**, 1912–1920.

26 J. Yang, S. Zhang, Z. Feng, Y. Cao and D. R. Zhu, Ba-MOFs with tetrazole-based acetic acids: unusual configuration, novel topology and high proton conductivity, *Dalton Trans.*, 2021, **50**, 11975–11985.

27 H. Okawa, K. Otsubo, Y. Yoshida and H. Kitagawa, Remarkably enhanced proton conduction of $NBu_2(CH_2COOH)_2[MnCr(ox)_3]$ by multiplication of carboxyl carrier in the cation, *Chem. Commun.*, 2020, **56**, 6138–6140.

28 Z. Q. Shi, N. N. Ji, M. H. Wang and G. Li, A comparative study of proton conduction between a 2D zinc(II) MOF and its corresponding organic ligand, *Inorg. Chem.*, 2020, **59**, 4781–4789.

29 G.-R. Si, F. Yang, T. He, X.-J. Kong, W. Wu, T.-C. Li, K. Wang and J.-R. Li, Enhancing proton conductivity in Zr-MOFs through tuning metal cluster connectivity, *J. Mater. Chem. A*, 2022, **10**, 1236–1240.

30 T.-E. Ho, A. Datta and H. M. Lee, Proton-conducting metal–organic frameworks with linkers containing anthracenyl and sulfonate groups, *CrystEngComm*, 2022, **24**, 5450–5459.

31 Y. Wang, J. Yin, D. Liu, C. Gao, Z. Kang, R. Wang, D. Sun and J. Jiang, Guest-tuned proton conductivity of a porphyrinylphosphonate-based hydrogen-bonded organic framework, *J. Mater. Chem. A*, 2021, **9**, 2683–2688.

32 Y. Huang, F. Zhou, J. Feng, H. Zhao, C. Qi, J. Ji, S. Bao and T. Zheng, An ultra-stable hafnium phosphonate MOF platform for comparing the proton conductivity of various guest molecules/ions, *Chem. Commun.*, 2021, **57**, 1238–1241.

33 L. Feng, T. Y. Zeng, H. B. Hou, H. Zhou and J. Tian, Theoretical hydrogen

bonding calculations and proton conduction for Eu(III)-based metal-organic framework, *RSC Adv.*, 2021, **11**, 11495–11499.

34 X. Chen, Z. Zhang, J. Chen, S. Sapchenko, X. Han, I. da-Silva, M. Li, I. J. Vitorica-Yrezabal, G. Whitehead, C. C. Tang, K. Awaga, S. Yang and M. Schroder, Enhanced proton conductivity in a flexible metal-organic framework promoted by single-crystal-to-single-crystal transformation, *Chem. Commun.*, 2021, **57**, 65–68.

35 Q. Wang, Z. Ye, G. Shi, K. Guo and G. Li, Proton conduction in two Cu/Zn dimer-based hydrogen-bonded supramolecular frameworks from imidazole multi-carboxylate, *New J. Chem.*, 2020, **44**, 8098–8105.

36 Y. Qin, M.-H. Xue, B.-H. Dou, Z.-B. Sun and G. Li, High protonic conduction in two metal–organic frameworks containing high-density carboxylic groups, *New J. Chem.*, 2020, **44**, 2741–2748.

37 F. Igoa, M. Romero, G. Peinado, J. Castiglioni, J. Gonzalez-Platas, R. Faccio, L. Suescun, C. Kremer and J. Torres, Ln(III)–Ni(II) heteropolynuclear metal organic frameworks of oxydiacetate with promising proton-conductive properties, *CrystEngComm*, 2020, **22**, 5638–5648.

38 L. Zhang, X. Liu, M. Shang, F. Sun, J. Jian, K. Bu, D. Zeng and H. Yuan, Efficient proton conductivity of a novel 3D open-framework vanadoborate with $[V_6B_{20}]$ architectures, *Dalton Trans.*, 2021, **50**, 3240–3246.

39 Y. Y. Enakieva, E. A. Zhigileva, A. N. Fitch, V. V. Chernyshev, I. A. Stenina, A. B. Yaroslavtsev, A. A. Sinelshchikova, K. A. Kovalenko, Y. G. Gorbunova and A. Y. Tsivadze, Proton conductivity as a function of the metal center in porphyrinylphosphonate-based MOFs, *Dalton Trans.*, 2021, **50**, 6549–6560.

40 C. Sun, C. M. Pask, S. T. Pham, E. Rapaccioli, A. J. Britton, S. Micklethwaite, A. Bell, M. O. Besenhard, R. Drummond-Brydson, K.-J. Wu and S. M. Collins, Modulating proton conductivity through crystal structure tuning in arenedisulfonate coordination polymers, *J. Mater. Chem. A*, 2024, **12**, 18440–18451.

41 F. Yang, X. J. Kong, T. He, Z. Zhang, K. Wang, H. Du, G. Cai, J. Ju, X. Wang, J. R. Li, J. Sun and C. Zhong, Solvent-free construction of Cr(III)-sulfonate coordination polymers, *Chem. Sci.*, 2025, **16**, 11823–11832.

42 X. Liang, K. Cai, F. Zhang, J. Liu and G. Zhu, One, two, and three-dimensional metal–organic coordination polymers derived from enantiopure organic phosphorate: homochirality, water stability and proton conduction, *CrystEngComm*, 2017, **19**, 6325–6332.

43 X. Liang, K. Cai, F. Zhang, J. Liu and G. Zhu, A proton-conductive lanthanide oxalatophosphonate framework featuring unique chemical stability: stabilities of bulk phase and surface structure, *J. Mater. Chem. A*, 2017, **5**, 25350–25358.

44 X. Liang, Y. Chen, L. Wang, F. Zhang, Z. Fan, T. Cao, Y. Cao, H. Zhu, X. He, B. Deng, Y. You, Y. Dong and Y. Zhao, Effect of carbon-skeleton isomerism on the dielectric properties and proton conduction of organic cocrystal compounds assembled from 1,2,4,5-benzenetetracarboxylic acid and piperazine derivatives, *New J. Chem.*, 2019, **43**, 11099–11112.

45 X. Liang, T. Cao, L. Wang, C. Zheng, Y. Zhao, F. Zhang, C. Wen, L. Feng and C. Wan, From an organic ligand to a metal–organic coordination polymer, and to a metal–organic coordination polymer–cocrystal composite: a continuous promotion of the proton conductivity of crystalline materials, *CrystEngComm*, 2020, **22**, 1414–1424.

46 F. Costantino, A. Donnadio and M. Casciola, Survey on the phase transitions and their effect on the ion-exchange and on the proton-conduction properties of a flexible and robust Zr phosphonate coordination polymer, *Inorg. Chem.*, 2012, **51**, 6992–7000.

47 D.-W. Fu, H.-Y. Ye, Q. Ye, K.-J. Pan and R.-G. Xiong, Ferroelectric metal–organic coordination polymer with a high dielectric constant, *Dalton Trans.*, 2008, 874–877.

48 A. Pathak, G. R. Chiou, N. R. Gade, M. Usman, S. Mendiratta, T. T. Luo, T. W. Tseng, J. W. Chen, F. R. Chen, K. H. Chen, L. C. Chen and K. L. Lu, High-kappa samarium-based metal-organic framework for gate dielectric applications, *ACS Appl. Mater. Interfaces*, 2017, **9**, 21872–21878.

49 S. Kamal, K. R. Chiou, B. Sainbileg, A. I. Inamdar, M. Usman, A. Pathak, T.-T. Luo, J.-W. Chen, M. Hayashi, C.-H. Hung and K.-L. Lu, Thermally stable indium based metal–organic frameworks with high dielectric permittivity, *J. Mater. Chem. C*, 2020, **8**, 9724–9733.

50 X. Peng, W. Xu, L. Chen, Y. Ding, S. Chen, X. Wang and H. Hou, Polyimide complexes with high dielectric performance: toward polymer film capacitor applications, *J. Mater. Chem. C*, 2016, **4**, 6452–6456.

51 R. Popielarz, C. K. Chiang, R. Nozaki and J. Obrzut, Dielectric properties of polymer/ferroelectric ceramic composites from 100 Hz to 10 GHz, *Macromolecules*, 2001, **34**, 5910–5915.

52 M. Sánchez-Andújar, S. Yáñez-Vilar, B. Pato-Doldán, C. Gómez-Aguirre, S.

Castro-García and M. A. Señarís-Rodríguez, Apparent colossal dielectric constants in nanoporous metal organic frameworks, *J. Phys. Chem. C*, 2012, **116**, 13026–13032.

53 L. H. Chen, J. B. Guo, X. Wang, X. W. Dong, H. X. Zhao, L. S. Long and L. S. Zheng, Giant room-temperature magnetodielectric response in a MOF at 0.1 Tesla, *Adv. Mater.*, 2017, **29***,* 1702512.

54 S. Mendiratta, M. Usman, T. W. Tseng, T. T. Luo, S. F. Lee, L. Zhao, M. K. Wu, M. M. Lee, S. S. Sun, Y. C. Lin and K. L. Lu, Low dielectric behavior of a robust, guest-free magnesium(II)–organic framework: a potential application of an alkaline-earth metal compound, *Eur. J. Inorg. Chem.*, 2015, **2015**, 1669–1674.

55 B.-T. Qu, J.-C. Lai, S. Liu, F. Liu, Y.-D. Gao and X.-Z. You, Cu- and Ag-based metal–organic frameworks with 4-pyranone-2,6-dicarboxylic acid: syntheses, crystal structures, and dielectric properties, *Cryst. Growth Des.*, 2015, **15**, 1707–1713.